Eu-doped Mg–Ni ferrites: a reliable strategy to enhance dielectric properties for high-frequency applications

Souhir Bouzidi, Najah Rhimi, Jamila Dhahri, Zouhaier Aloui, Abdelaziz Bouazizi, Kamel Khirouni, Malek Gassoumi, Jean Juraszek

Eu-Doped Mg-Ni Ferrites: A Reliable Strategy to Enhance Dielectric Properties for High-Frequency Applications

Souhir Bouzidi[1], Najah Rhimi[1*], Jamila Dhahri[2], Zouhaier Aloui[3], Abdelaziz Bouazizi[1], Kamel Khirouni[4], Malek Gassoumi[1], Jean Juraszek[5]

[1]Laboratoire de La Matière Condensée et des Nanosciences, Faculté Des Sciences de Monastir, Université de Monastir, 5000, Monastir, Tunisia
[2]Laboratory of Physical Chemistry of Materials, Physics Department, Faculty of Sciences of Monastir, Monastir University, 5019, Monastir, Tunisia
[3]Chemistry Department, College of Science, King Khalid University (KKU), Abha 61413, P.O. Box 9004, Saudi Arabia
[4]Laboratory of Physics of Materials and Nanomaterials Applied to the Environment (LaPHYMNE), Faculty of Sciences of Gabès cited Erriadh, 6079 Gabès, Tunisia
[5]Univ Rouen Normandie, INSA Rouen Normandie, CNRS, Normandie Univ, GPM, UMR 6634, F-76000, Rouen, France

Corresponding authors: malek.gassoumi@gmail.com

najahrhimi880@gmail.com

Published in : *Journal of Materials Science: Materials in Electronics*, 2024, 36 (1), pp.32. ⟨10.1007/s10854-024-14058-2⟩

Abstract

In this study, we synthesized $Mg_{0.5}Ni_{0.5}Fe_2O_4$ (MNFO) spinel ferrites and Eu-doped spinel $Mg_{0.5}Ni_{0.5}Fe_{1.98}Eu_{0.02}O_4$ (MNFEuO) using a solid-state method. Our comprehensive analysis included structural, morphological, and dielectric properties. X-ray diffraction (XRD) confirmed the cubic structure of both MNFO and MNFEuO. The Rietveld refinement revealed an increased lattice constant for the Eu-doped sample, attributed to the larger ionic radius of Eu^{3+} ions. The crystallite size was 46 nm for MNFO and 80 nm for MNFEuO. The bulk densities were measured as 4.32 g/cm³ for MNFO and 4.41 g/cm³ for MNFEuO, with the theoretical densities calculated as 4.96 g/cm³ and 4.98 g/cm³, respectively. Scanning electron microscopy (SEM) indicated well-defined, spherical particles with uniform size distribution and average grain sizes of 0.86 µm for MNFO and 0.62 µm for MNFEuO. X-ray photoelectron spectroscopy (XPS) confirmed the purity and oxidation states of the elements. Impedance spectroscopy showed a significant enhancement in conductivity for MNFEuO, with DC conductivity values at 600 K of 57×10^{-4} S.m^{-1} for MNFO and 107.4×10^{-4} S.m^{-1} for MNFEuO, indicating superior electrical performance in the doped sample. Dielectric

analysis demonstrated an increase in the dielectric constant for MNFEuO compared to MNFO, suggesting improved polarization properties. These findings indicate that Eu-doped spinel ferrites possess promising potential for high-frequency and advanced electronic applications.

Keywords: Ferrites, MEB, XPS, XRD, Electrical and dielectric analysis

1. Introduction

In recent years, significant attention has been dedicated to the development of novel materials, driven by their potential for various industrial applications [1-8]. Researchers across materials science, engineering, and physics fields have been particularly focused on understanding and enhancing the dielectric and electrical properties of these materials to support technological advancements. Among these innovations, ceramic materials have shown remarkable promise, especially for electronic applications, such as ceramic capacitors and varistors. Within the ceramic family, recent studies such as doped $ACu_3Ti_4O_{12}$ [9-12], and co-modified TiO_2 [13] ceramics, demonstrating their potential in electronic device applications due to improved stability and performance. Our research has specifically concentrated on ceramics, particularly spinel structures, as we explore their unique properties and potential applications in next-generation electronic technologies. Spinel ferrites belong to a class of ceramic materials characterized by the generic formula AFe_2O_4, where A represents a divalent metal such as magnesium, cobalt, iron, copper, nickel…. The crystal structure of spinel ferrite consists of a cubic-closed arrangement of oxygen ions, featuring 8 tetrahedral (A-site) and 16 octahedral interstitials (B-site) positions within the unit cell [14, 15]. Generally, there exist three varieties of spinel ferrite. A typical spinel can be denoted as $\left(A^{II}\right)^{tet}\left(B^{III}\right)_2^{oct}O_4$. In an inverse spinel arrangement, the A^{II} ions fill the octahedral sites while a portion of the B^{III} ions occupies the tetrahedral sites. This configuration can be symbolized as $\left(B^{III}\right)^{tet}\left(A^{II}B^{III}\right)_2^{oct}O_4$. Finally, in mixed spinel ferrite, both A^{II} and B^{III} ions occupy octahedral and tetrahedral sites. This configuration can be symbolized as $\left(A^{II}B^{III}\right)^{tet}\left(A^{II}B^{III}\right)_2^{oct}O_4$. The physical and chemical characteristics of ferrites are influenced by some variables such as heating and cooling rates, sintering temperature and time. A range of techniques, including the solvent evaporation method, the ceramic method, the hydrothermal method, the sol-gel method and the citrate

method, are employed to synthesis spinel ferrites. Ferrite nanoparticles have attracted the attention of scientists in the field of technical materials because of their exceptional electrical properties and remarkable chemical and thermal stability. These nanoparticles are distinguished by their straightforward synthesis, exceptional electrical conductivity, minimal electrical losses, and inherent lack of toxicity, making them valuable for various technological applications across different fields [16, 17]. These applications cover magnetic recording devices, television manufacturing, biomedical applications, transformer design, electrochemical energy storage [18-20]. $MgFe_2O_4$ is an important structure of the spinel family. Its crystalline composition adheres to the typical cubic form. It has considerable utility in diverse fields such as heterogeneous catalysis, anode materials for batteries, magnetic technologies, sensors and adsorption. The arrangement of cations in magnesium ferrite can be represented by $\left(Mg_{1-x}^{2+}Fe_{x}^{3+}\right)_{A}\left[Mg_{x}^{2+}Fe_{2-x}^{3+}\right]_{B}O_{4}^{2-}$,with "x" indicating the degree of cation inversion in the structural lattice [21]. Conversely, there has been significant interest in Ni-Mg ferrite compounds. Consequently, among spinel ferrites, $Ni_{1-x}Mg_xFe_2O_4$ ferrite has garnered attention for its notable attributes, such as elevated electrical resistivity, low coercivity, chemical stability, and cost-effectiveness, which have led to increased interest in the large-scale synthesis of ferrite materials for industrial use. $Ni_{1-x}Mg_xFe_2O_4$ ferrites are also esteemed for their suitability in high-frequency applications and magnetodielectric properties, particularly in the microwave and radio frequency spectrum [22]. Studies have demonstrated that among various compositions, $Ni_{0.6}Mg_{0.4}Fe_2O_4$ exhibits relatively superior electrical-magnetic characteristics [23]. The $Ni_{1-x}Mg_xFe_2O_4$ sample has been researched and reported in several research projects [23-26]. Several scientists have investigated how the substitution of certain elements in Ni-Mg spinel ferrite can improve its physical properties. They have studied the properties of spinel ferrites by introducing various more important rare-earth ions into the material. The use of europium doped copper ferrites in high-frequency applications is important because of its significant physical effects, including minimal dielectric loss, important sensing capabilities and low conductivity levels. M.S. Sikder et al. [27] demonstrated that by incorporating Eu concentration, both the magnetic loss and dielectric loss decreased. This resulted in Eu-doped samples exhibiting superior dielectric and magnetic quality factors compared to the undoped one. Additionally, the introduction of Eu content in the sample led to increased resistivity and impedance. In addition, I. Sardar et al. [28]

indicates that the permeability and dielectric measurements exhibit an enhanced quality factor in the Eu-doped samples, accompanied by reduced dielectric losses. Additionally, analysis of frequency-dependent resistivity and impedance indicates an improvement in their characteristics. J. Mahapatro et al. [29] indicate that incorporating Eu^{3+} ions through doping leads to an increase in the dielectric constant. Consequently, the materials exhibit potential suitability for applications in microwave devices. Furthermore, Shilpa Kumari [30] illustrate that the introduction of Eu into $LaMnO_3$ oxide induces an increase in the dielectric constant and modulus, with the enhancement becoming more pronounced as the concentration of Eu increases. While doping with rare-earth elements such as europium (Eu^{3+}) has been studied to enhance these properties, there remains limited research on the detailed effects of Eu^{3+} doping in Ni-Mg spinel ferrites, particularly in terms of frequency-dependent dielectric behaviour and impedance characteristics. This study aims to address this gap by investigating the structural, morphological, and dielectric properties of Eu^{3+}-doped ferrite, providing new insights for its potential applications in advanced electronic and microwave technologies. The current study involved synthesizing spinel ferrites with the primary composition $Mg_{0.5}Ni_{0.5}Fe_2O_4$ (MNFO) through a solid-state technique. Subsequently, Eu^{3+} ions were introduced to create a doped spinel variant, denoted as $Mg_{0.5}Ni_{0.5}Fe_{1.98}Eu_{0.02}O_4$ (MNFEuO).

2. Experimental details

The MNFO and MNFEuO samples were elaborated using the solid-state method. Stoichiometric quantities of Magnesium oxide [MgO] (Sigma Aldrich, 99.99%), Iron oxide (III) [Fe_2O_3] (Sigma Aldrich, 99.99%), Nickel oxide [NiO] (Sigma Aldrich, 99.99%) and Europium oxide [Eu_2O_3] (Sigma Aldrich, 99.99%) were chosen to start our samples preparation. The powders were mixed and grounded. The milling process is done manually in ethanol for 30 minutes using an agate mortar to homogenize the mixture. This step is essential to obtain uniform distribution of precursors. Then, the mixtures were calcined at 900 °C for 24 hours to ensure the chemical reaction between the components. The calcined mixtures were grounded again and calcined at 1100 °C for 12 hours to reduce grain size, homogenize powder and increase grain reactivity. Once thoroughly mixed, the powders were compressed into pellets with a diameter of 8 mm and a thickness of 2 mm using a pressing force of approximately 200 MPa and

sintered at 1200°C for 12 hours. All steps of the experimental procedure are described in **Figure 1**.

In order to confirm the cubic structure of the samples, X-ray diffraction (XRD) analysis was generated using a Panalytical X'Pert Pro system with Cu-Kα radiation (10° < 2$\boldsymbol{\theta}$ <90°). The morphological examination was performed utilizing a Scanning Electronic Microscope (SEM) type JEOL JSM.6390L. In addition, Thermo-Scientific K-ALPHA instrument was used to investigate the chemical surface. The electrical and dielectric features of the prepared ferrites were assessed employing the "N4L-NumetriQ" impedance analyzer. These analyses were carried out over a temperature range from 380 to 640 K, while measurements were collected over a wide frequency spectrum from 10^2 to 10^7 Hz.

3. Results and Discussions

3.1. Structural analysis

The X-ray diffraction (XRD) patterns for MNFO and MNFEuO samples were measured at room temperature, covering a 2θ range of 10° to 90°, and displayed in **Figure 2(a, b)**. As we can see, the diffraction peaks (111), (220), (311), (222), (400), (422), (333), (511), (440), (531), (620) and (533) were indexed in the cubic structure with the $Fd\bar{3}m$ space group. In addition, for the doped sample, a secondary phase was detected which, attributed to $EuFeO_3$ with an orthorhombic system with space group Pnma. The presence of the $EuFeO_3$ orthoferrite phase as an impurity in the XRD analysis can be attributed to an excess of Eu^{3+} ions, which may lead to the formation of the Eu_2O_3 phase along grain boundaries. This type of impurity has been observed by P. Sivaprakash et al. **[31]**. The quantity and nature of the dopant (Eu^{3+}) significantly influence the development of secondary phases during the sintering process. Introducing small amounts of Eu^{3+} ions into spinel ferrite can modify both the matrix size and phase composition. Due to the larger ionic radius of Eu^{3+} (1.066 Å) compared to Fe^{3+} (0.645 Å) **[32]**, Eu^{3+} ions can partially substitute for Fe^{3+} ions at the octahedral sites within the spinel structure. This difference in ionic size promotes the formation of the $EuFeO_3$ phase in our sample, as any excess Eu^{3+} ions tend to form Eu_2O_3 along grain boundaries.

The Rietveld refinement analysis of MNFO and MNFEuO powders was performed using the FullProf software **[33]**. Peak shapes were refined utilizing the Pseudo-Voigt function, while the background was modelled via linear interpolation between set

background points with adjustable heights. A high-quality fit was observed between the measured and calculated patterns, confirming the presence of the cubic phase. Detailed refinement results are provided in **Table 1**. Compared to the pure ferrite, the substitution of Eu^{3+} ion in MNFO resulted in an increase in lattice the cubic cell volume. This result was confirmed by the shift of the (311) peak forward towards lower 2θ angles **Figure 2(c)**. Further, the ionic radius of Eu^{3+} ions (1.066 Å) is larger than that of Fe^{3+} ions (0.645 Å) **[32]**. The substitution of Fe^{3+} ions with Er^{3+} ions suggests that Eu^{3+} ions occupy the B site lattice with sufficient space. Consequently, this leads to the expansion of the unit cell, resulting in an increase in the lattice constants of the MNFEuO sample. The same behaviour is reported by R. Tholkappiyan et al. **[34]**.

MNFO and MNFEuO samples have mix spinel structures in which Ni^{2+} **[35]** and Eu^{3+} ions prefer octahedral sites, while Mg^{2+} and $Fe^{3+/2+}$ ions prefer both tetrahedral and octahedral sites **[36, 37]**. Hence, the distribution of cations in the prepared samples may be suggested as **[38]**:

$$\left(Mg^{2+}_{y-x}Fe^{3+}_{1-y+x}\right)_A\left[Ni^{2+}_{0.5-y}Mg^{2+}_{0.5-y}Fe^{3+}_{1+y+x}Eu^{3+}_{x}\right]_B O^{2-}_4 \quad (1)$$

Here, y is the degree of inversion and x is the concentration of Eu^{3+} (x=0 and 0.02) and A and B are tetrahedral and octahedral sites, respectively.

The most intense peak (311) was used to determine full width at half maxima $\beta_{(311)}$ which, is used to estimate the crystallite size via the Scherrer's formula **[39]**:

$$D_C = \frac{0.89\lambda}{\beta_{(311)}\cos\theta_{(311)}} \quad (2)$$

λ= 1.5406 Å represents the wavelength of CuKα radiation and $\theta_{(311)}$ denotes the angle of the most intense (311) peak. The calculated crystallite size is 46 nm and 80 nm for the MNFO and MNFEuO samples, respectively, which confirms that our samples are of nanometer dimensions.

The bulk density ρ_b of the MNFO and MNFEuO ferrites was determined using geometric measurement techniques, which involve calculating the density based on the mass and dimensions of the samples. The measured bulk density of MNFO was found to be 4.32 g/cm³, while MNFEuO exhibited a slightly higher bulk density of 4.41 g/cm³. This difference may indicate variations in the compactness and structural characteristics of the two ferrite compositions. To complement these measurements, the theoretical density ρ_{th} was calculated using the formula **[40]**:

$$\rho_{th} = \frac{ZM}{Na^3} \quad (3)$$

In this equation, M represents the molecular weight of the specific ferrite composition, N denotes Avogadro's number, a^3 indicates the volume of the cubic unit cell, and Z refers to the number of molecules per unit cell, which is 8 for the spinel structure. For MNFO, the ρ_{th} was calculated to be 4.96 g/cm³, whereas MNFEuO had a ρ_{th} of 4.98 g/cm³. The increase in ρ_{th} upon doping with Eu^{3+} can be attributed to the atomic weight and density of Eu^{3+} (151.96 g/mol and 5.24 g/cm³, respectively) [41], which are significantly higher than those of Mg^{2+} (24.31 g/mol and 1.74 g/cm³), Ni^{2+} (58.69 g/mol and 8.90 g/cm³) and Fe^{3+} (5.85 and 7.86 gm/cm^3) [42, 43]. Further, the bulk density is lower than the X-ray density. This may be due to the existence of pores which were formed and developed during the sample preparation or the sintering process.

To assess the packing efficiency of these materials, the relative density ρ_r was determined using the following equation [44]:

$$\rho_r = \frac{\rho_b}{\rho_{th}} \times 100 \quad (4)$$

The relative density was calculated to be approximately 87% and 89 % for MNFO and MNFEuO, respectively, indicating that both samples occupy a significant portion of the theoretical density. This percentage reflects a relatively high level of densification, suggesting effective processing conditions.

3.2. Morphological analysis

The SEM images of the MNFO and MNFEuO ceramics provide insights into the microstructural characteristics of the synthesized materials **Figure 3(a, b)**. It reveals well-defined particles with a relatively uniform size distribution, indicating a consistent synthesis process. The particles predominantly exhibit a spherical morphology, with few pores and sharply defined grain boundaries. Notably, the inclusion of Eu^{3+} ion into MNFO matrix did not cause any changes on the sample morphology. The average grain size was estimated using ImageJ software and the data were fitted using the Log-Normal function [45]:

$$f(D_G) = \frac{1}{\sqrt{2\pi}\sigma D_G} e^{-\left[\frac{\ln\left(\frac{D_G}{D_0}\right)^2}{2\sigma^2}\right]} \quad (5)$$

D_0 represents the median diameter, and σ corresponds to the data dispersion. The inset of **Figure 3(a, b)** illustrates the histograms of average grains size for both samples. The D_G is equal to 0.86 and 0.62 µm for MNFO and MNFEuO ceramics, respectively. The empirical data indicate that the Eu^{3+} substitution inhibits the growth of crystalline particles, as shown by a noticeable reduction in the average size of the ferrite grains. This reduction in grain size can likely be explained by the stronger bond energy of Eu^{3+}-O^{2-} compared to Fe^{3+}-O^{2-}. This stronger bond energy lowers the energy required for grain growth, resulting in a more refined grain structure **[46, 47]**.

The grain sizes determined using Scherrer's method are smaller than those observed in the SEM images. This discrepancy can be attributed to the fact that each particle seen in the SEM is composed of multiple crystallized grains.

To confirm the presence of all elements in our MNFEuO sample, energy-dispersive X-ray (EDX) analysis was performed, as shown in **Figure 3(c)**. All elements from the various precursors were detected, validating the effectiveness of the process used to produce the ceramic. Additionally, the EDX spectrum reveals a characteristic Eu^{3+} peak at 5.84 keV, confirming the incorporation of Eu^{3+} into MNFO. The elemental mapping of the MNFEuO surface in Figure (c) further demonstrates a homogeneous distribution of all elements across the ceramic surface.

3.3. XPS analysis

X-ray Photoelectron Spectroscopy (XPS) represents an effective methodology, not only for the detection of chemical elements but also facilitating quantitative analysis of the oxidation states of metal ions within synthesized materials. **Figure 4** depicted the XPS spectra for the MNFO and MNFEuO samples at room temperature. The appearance of the C1s peak within the wide spectra can be linked to hydrocarbon contamination from the laboratory environment, contributing to the C-C band **[48]**. Consequently, this observed peak serves as an energy reference for the determination of core-level spectra peak positions. Furthermore, elemental species such as Mg, Ni, Fe, Eu, and O were successfully identified, thereby validating the purity of the synthesized samples. Detailed information regarding peak positions and Full Width at Half Maximum (FWHM) for core-level spectra, including Mg2p, Ni2p, Fe2p, Eu3d, and O1s are provided in Tables 4 and 5, respectively, for the synthesized materials. A detailed examination of the XPS spectra was employed to confirm the electron configuration and the level of oxidation of the constituent elements within the samples. A Shirley

background correction method was used, while parameters such as full width at half maximum (FWHM) and peak positions were permitted to adjust. The selection of the optimal number of peaks for fitting was carried out manually, with preference given to the fewest peaks that gave a satisfactory fit for the analysis. The values corresponding to the observed peaks are summarized in **Table 2**.

- **Mg1s peak**

The analysis of the Mg1s peak is required to elucidate the cation distribution of Mg ions within the two samples. **Figure 5(a, b)** illustrates the high-resolution Mg1s spectra of both MNFO and MNFEuO compounds. The Mg1s spectra of pure ferrite can be fitted into two binding energies at 1303.21 eV and 1305.74 eV, characteristic of the Mg^{2+} ion **[49]**. However, in the case of doped ferrite, the Mg1s spectra can be fitted into two binding energies at 1302.95 eV and 1306.04 eV, which assigned to the Mg^{2+} ion **[49]**. In addition, Typically, in ferrites, when cations are distributed across two different sites, the appearance of two XPS peaks, peak broadening, and peak shift of the photoelectron peak is noted within the Eu^{3+} doping, which attributed to the distribution of Mg ions in octahedral and tetrahedral sites within the ferrite lattice. The peak at higher binding energy corresponds to octahedral Mg ions, while the peak at lower binding energy is associated with Mg ions in the tetrahedral site. This widening of the peak could be attributed to the incorporation of Eu^{3+} ions into the spinel structure. Furthermore, it suggests a cation distribution of Mg ions across octahedral and tetrahedral sites, influenced by the presence of Eu^{3+} ions. This result confirms the XRD study.

- **Ni2p peak**

Figure 5(c, d) displays the Ni2p core level spectra of the MNFO and MNFEuO samples. The Ni2p spectra are characteristic of Ni^{2+} with the $Ni2p_{3/2}$ and $Ni2p_{1/2}$ peaks at 856.31 and 873.19 eV for MNFO and at 856.50 and 873.43 eV for MNFEuO, respectively, accompanied by satellite peaks located at 864.11 and 864.07 eV **[50, 51]**. These satellite peaks are typically seen in paramagnetic Ni^{2+} compounds and are attributed to charge transfer multielectron transitions **[52, 53]**. It should be noted that the difference between the $Ni2p_{3/2}$ and $Ni2p_{1/2}$ levels align well with those reported in references **[52]**.

- **Fe2p peak**

According to the spin-orbit coupling principle, the Fe2p orbital displays a $Fe2p_{3/2}$ and $Fe2p_{1/2}$ doublet, assigned to the exchange interaction between the outer 3d electrons and the remaining 3s electron of the atom [54]. Figure 5(e, f) depicts the high-resolution XPS spectra of the Fe2p peak for both pure ferrite and Eu-doped ferrite. The doublet peaks attributed to Fe $2p_{3/2}$ and Fe $2p_{1/2}$ and observed at binding energies near 712.33 eV and 725.94 eV for MNFO and 712.64 eV and 726.06 eV for MNFEuO may be ascribed to are Fe^{3+} and Fe^{2+}, respectively [55]. Furthermore, the broadening of the $Fe2p_{3/2}$ peak is evident upon doping pure ferrite with Eu^{3+}. This increase of the peak width arises from the distribution of Fe^{3+} cations across both octahedral and tetrahedral sites within the spinel lattice, a distribution influenced by the presence of Eu in the sample. Notably, the peak area corresponding to the distribution of Fe^{3+} in the octahedral site is high compared to that in the tetrahedral site. Europium is always preferred the octahedral sites. Consequently, Fe^{3+} ions can occupy both types of sites, thus distributing themselves between it, a phenomenon consistent with the findings from XRD analysis.

- **Eu3d peak**

Figure 5(g) displays the XPS spectra of Eu3d for MNFEuO sample. The presence of two distinct peaks at 1166.44 and 1137.15 eV corresponds to the core levels of $Eu3d_{3/2}$ and $Eu3d_{5/2}$, respectively, indicating that the Europium element is in the +3-oxidation state [56].

- **O1s peak**

The O1s spectra for MNFO and MNFEuO samples are shown in Figure 5(i, g). It can be fitted into two peaks in binding energy scope at 529.57 eV and 532.28 eV MNFO and 529.92 eV and 532.39 eV for MNFEuO, corresponding to lattice oxygen O^{2-} [57-59]. Additionally, the peak at 529.92 eV matches the previously reported data for Fe-O bonding [60]. This assignment of the photoelectron peak indicates that six oxygen ions are octahedrally coordinated with Fe(III).

3.4. Conductivity analysis

The measurements carried out by impedance spectroscopy allow calculating conductivity using the following formula [61]:

$$\boldsymbol{\sigma_{tot}} = \frac{\mathbf{G \times e}}{\mathbf{A}} \textbf{(6)}$$

Where G, e and A represent the conductance, thickness and surface area of the samples, respectively. The variation of conductivity as a function of frequency at different temperatures for the MNFO and MNFEuO compounds is represented in **Figure 6(a, b)**. At low frequencies, the conductivity exhibits a plateau-like behavior, showing slight temperature dependence and independence from frequency up to a value denoted as the "hopping frequency." This corresponds to direct current conductivity σ_{DC} which is due to band conduction [62]. At high frequencies, starting from the hopping frequency, conductivity begins to increase with both temperature and frequency. This corresponds to alternating current conductivity σ_{AC}. Several theories have been proposed for the study of σ_{AC}, among which is the site-to-site hopping model [63]. For our studied materials, the σ_{AC} is due to the electron hopping process between Fe^{3+} and Fe^{2+} ions in the octahedral site [64]. Jonscher suggested that dispersion is a 'universal' property of dielectric materials and a consequence of the complex interactions between mobile species [65]. It is worth mentioning that several authors have obtained AC conductivity by subtracting direct current (DC) conductivity from total conductivity, assuming that AC and DC processes originate from separate mechanisms. The frequency dependence of σ_{AC} is given by the following equation [39]:

$$\boldsymbol{\sigma_{tot} = \sigma_{dc}(T) + \sigma_{AC}(T, \omega) = \sigma_{dc} + \Upsilon \omega^{n}} \textbf{(7)}$$

Where ω is the angular frequency (ω=2πF), Υ represent a parameter which, varies with temperature and provides insights into the polarizability strength and n is an exponent which characterizes the extent of interaction between mobile charge carriers and their surroundings, with values ranging between 0 and 1. These interactions may manifest as either translational or localized phenomena [66]. The conductivity fitting using **Equation 7** demonstrates good agreement between experimental and theoretical curves for the studied materials. The evolution of the exponent n as a function of temperature for both samples is depicted in **Figure 7**. As can be seen, the values of 'n' exhibit a decline until reaching a minimum, followed by an increase with temperature increase. This observed behavior suggests that the Overlapping-Large Polaron Tunneling (OLPT) model emerges as the most appropriate framework for elucidating the electrical conduction mechanism within our materials [67]. The same behaviour was observed in the work of M. Chebbi et al. [68] for $Mg_{0.6}Co_{0.4}FeCrO_4$ Ferrites. This model elucidates

the mechanism of large polaron hopping. In essence, it implies the migration of polarons within the crystalline lattice. With its low effective mass and large radius, the movement from one site to another is easy. This process induces only minor reorganizations of the polarizability.

Figure 8(a) depicts the experimental curve illustrating the thermal variation of σ_{DC} for the MNFO and MNFEuO compounds. The increase in conductivity with temperature confirms the semiconductor behaviour **[69]**. The comparison of σ_{DC} values at 600 K for our samples, with respective values of 57×10^{-4} S.m^{-1} and 107.4×10^{-4} S.m^{-1}, to those reported in the literature reveals notable differences **[70, 71] (Figure 9(b))**. Our samples exhibit significantly higher conductivity compared to MCFC900 ($Mg_{0.6}Cu_{0.4}FeCrO_4$: 1.238×10^{-4} S.m^{-1}), MCFC1100 ($Mg_{0.6}Cu_{0.4}FeCrO_4$: 19×10^{-4} S.m^{-1}), MCCFC900 ($Mg_{0.6}Co_{0.2}Cu_{0.2}FeCrO$ sintered at 900°C: 1.49×10^{-4} S.m^{-1}) and MCCFC1100 ($Mg_{0.6}Co_{0.2}Cu_{0.2}FeCrO$ sintered at 1100°C: 7.042×10^{-4} S.m^{-1}), suggesting superior electrical performance in our compositions. These enhanced conduction properties contribute to improved charge carrier mobility and conductivity in our samples. Such superior conductivity in our compounds holds promising implications for their application in various electronic devices.

In the temperature range (380 – 480 K), denoted Region I, the experimental data may be fitted by Mott's Variable Range Hopping (VRH) law **[72]**:

$$\sigma_{DC} = \sigma_0 e^{\left(\frac{T_0}{T}\right)^{0.25}} \quad (8)$$

σ_0 represents a pre-exponential factor and T_0 denotes Mott's distinctive temperature parameter. This latter characterizes the transition between distinct transport mechanisms within the VRH model. Below T_0, the conduction primarily arises from hopping between localized states, resulting in conductivity exhibiting an exponential relationship with temperature due to thermally stimulated hopping. As temperature decreases towards T_0, both hopping distance and energy barriers diminish. Conversely, above T_0, the VRH mechanism changes, causing conductivity to deviate from exponential dependence. In this regime, charge carriers can access states farther away, leading to hopping distances comparable to the localization length **[73]**. **Figure 9(a)** displays the Ln(σ_{Dc}) variation versus $T^{-0.25}$, confirming the presence of VRH model at low temperatures, with T_0 estimated at 237×10^8 K and 5×10^8 K from the linear fit

for pure and doped samples. These T_0 values align well with those reported early [74-76]. Further, to find the activation energy values in this temperature range, the following expression is used [77]:

$$\mathbf{E_{a\sigma}} = \frac{3}{4\pi d^3 \rho_{EF}} \textbf{(9)}$$

d is the hopping distance and ρ_{EF} represents the density of states near the Fermi level, which can be expressed by the following expressions [72]:

$$\boldsymbol{\rho_{EF}} = \frac{24}{\pi \beta^3 K_B T_0} \textbf{(10)}$$

$$\mathbf{d^4} = \frac{9\beta}{8\pi K_B T \rho_{EF}} \textbf{(11)}$$

Here, β =1 nm represents the degree of localization [78] and $\boldsymbol{\rho_{EF}}$ is the density of the states near the Fermi level. **Table 3** presents the estimated values of T_0 and $\boldsymbol{\rho_{EF}}$ for both samples. In comparison with pure ferrite, the $\boldsymbol{\rho_{EF}}$ values increased from 3.74×10^{15} to $1.77 \times 10^{17} eV^{-1} cm^{-3}$ with the doping of Eu^{2+}, leading to increased distortion in the states near the Fermi level in regions I. This increase can be attributed to the enhancement of the conductivity with doping Eu^{2+} in the MNFO composition [78]. **Figure 9(b)** illustrates the temperature-dependent trend of the hopping distance d, indicating a reduction from 0.075 to 0.071 nm and from 0.083 to 0.079 nm for pure and doped samples, respectively. The Mott parameters obtained from our study exhibit favourable comparison with those reported in reference [78] for nano-ferrite samples. From the observed values of the hopping distance d and the density of states near the Fermi level $\boldsymbol{\rho_{EF}}$, the activation energy $E_{a\sigma}$ was computed. The **Figure 9(c)** shows the temperature profile of the activation energy within the range of 380–480 K. Notably, there is a discernible rise in $E_{a\sigma}$ from 0.15 to 0.18 eV and 0.028 to 0.030 eV as the temperature increases for MNFO and MNFEuO samples, respectively. This observed trend aligns with the characteristic behavior exhibited by similar disordered materials [79].

In the temperature range (500 – 640 K), denoted Region II, the experimental data can be fitted by the Arrhenius law [80]:

$$\boldsymbol{\sigma_{DC}} = \boldsymbol{\sigma_0 e^{-\frac{E_{a\sigma}}{K_B T}}} \textbf{(12)}$$

Figure 10 depicts the variation of Ln(σ_{DC}) as a function of 1000/T for MNFO and MNFEuO samples. A decreasing linear trend is observed. The activation energy values are deduced from the slope, $E_{a\sigma}$ = 0.649 eV and 0.586 for MNFO and MNFEuO, respectively. The conductivity can be described by small polaron hopping (SPH). Increasing the temperature lowers one side of the potential well, enhancing the hopping of charge carriers to neighboring sites. Consequently, the number of polarons increases, leading to an increase in conductivity, confirming that the conduction process is thermally activated. The activation energy values are associated with doubly ionized oxygen vacancies ($V_O^{\bullet\bullet}$) **[81]**.

3.5. Complex impedance spectra

Nyquist plots are employed to analyse electrical properties, where the complex impedance Z = Z' ± Z'' is plotted in the complex plane as (x = Z') and (y = ± Z''). **Figure 11(a, b)** depicts Nyquist diagrams obtained for MNFO and MNFEuO samples in the temperature range 380-640K. These curves exhibit a single semi-circular arc in the studied frequency range. It is observed that the radii of the semicircles decrease as temperature increases, indicating the semiconducting nature of both samples **[39, 82-83]**. To extract the characteristic parameters, equivalent circuits were utilized using the Z-view software **[84]**. The equivalent circuit enables the simulation of all impedance spectra for the temperature range of 380-640 K for both compounds. The modelled equivalent circuit was represented in **Figure 12**. The parameters extracted from the equivalent electrical circuit are the polarization resistance (R_p), describes the electrical resistance of the material, and the parameters of the Constant Phase Element (CPE) which, is used instead of a pure capacitance to account for the offset associated with the electrical inhomogeneity of the material (distribution of relaxation times of the system). The CPE impedance is given by the following expression **[85]**:

$$\mathbf{Z_{CPE}} = \frac{\mathbf{1}}{\mathbf{T(j\omega)^P}} \quad \mathbf{(13)}$$

Where T (CPE-T) is expressed in capacitance units. Generally, the impedance Z_{CPE} is considered a dispersive capacitance. The value of the exponent P (CPE-P) determines the capacitive nature of the element: if P=1, the CPE is an ideal capacitance; if P=0, the CPE behaves like a pure resistance, whereas if P=-1, it behaves like an inductance and has a Warburg element when P=0.5. The total complex impedance of the proposed equivalent circuit is expressed as:

$$Z^* = Z' - jZ'' \quad (14)$$

Where Z' and Z'' are expressed by the following formulae:

$$Z' = \frac{R_p(1+R_pT\omega^P\cos(\frac{P\pi}{2}))}{(1+R_pT\omega^P\cos(\frac{P\pi}{2}))^2+(R_pT\omega^P\sin(\frac{P\pi}{2}))^2} \quad (15)$$

and,

$$-Z'' = \frac{R_p{}^2T\omega^P\sin(\frac{P\pi}{2})}{(1+R_pT\omega^P\cos(\frac{P\pi}{2}))^2+(R_pT\omega^P\sin(\frac{P\pi}{2}))^2} \quad (16)$$

The values of R_p, CPE-T, and CPE-P are adjusted using the least squares method, which minimizes the gap between experimental and calculated values. The limit of Z' at low frequencies is R_p, deduced from the intersection of the representative circle of Z' with the real axis at high Z values. The modelled values of R_p, CPE-T, and CPE-P are listed in **Table 4**. For all three compounds and at various temperatures, the values of the CPE-T capacitance are on the order of nF, indicating that the observed semicircles are attributed to intergranular conduction **[86, 87]**.

3.6. Impedance analysis

Figure 13(a, b) illustrates the variation of the real part of complex impedance Z' as a function of frequency for MNFO and MNFEuO. For the two samples, the frequency response of Z' exhibits similar trends. It is observed that at low temperatures and frequencies, the values of Z' are typically high. The Z' gradually decreases until reaching a critical value, beyond which it decreases to zero at high frequencies. At high frequency, the values of Z' converge. These results can be explained by the charges released due to the reduction of the material barrier with increasing temperature. At high frequencies and for all temperatures, the narrowing of Z' values can be interpreted by the presence of a space charge region following the reduction of the materials' resistive behaviour **[88]**. However, a similar observation was reported by M. L. Bouazizi et al. **[89]** for the compound $Ni_{0.6}Mg_{0.2}Co_{0.2}FeCrO_4$.

Figure 14(a, b) represent the variation of the imaginary part of complex impedance Z'' as a function of frequency at different temperatures for the two samples. It is noticeable that all samples exhibit the emergence of a maximum Z''_{max} that shifts towards higher frequencies with increasing temperature. The displacement of this maximum confirms the existence of a potential relaxation phenomenon **[90]**. Similar behavior has been

observed by M. Chebbi et al. [91] for spinel ferrites $Mg_{0.6}Co_{0.4}FeCrO_4$. From the maximum of Z", the relaxation frequency F_z of charge carriers can be deduced, and subsequently the relaxation time τ_z using the following expression:

$$\boldsymbol{\tau_z = \frac{1}{2\pi F_z}} \quad \textbf{(17)}$$

The variation of the τ_z as a function of 1000/T is characterized by an Arrhenius-type behavior:

$$\boldsymbol{\tau_z = \tau_0 e^{-\frac{E_{az}}{K_B T}}} \quad \textbf{(18)}$$

τ_0 is the pre-exponential factor or the characteristic relaxation time constant, and E_{az} represent the activation energy. In **Figure 15**, we have plotted Ln(τ_z) versus f(1000/T) for the MNFO and MNFEuO compounds, demonstrating that it can be well fitted by a linear fit. The activation energies obtained are summarized in **Table 5**. The activation energy values are associated with doubly ionized oxygen vacancies ($V_O^{\bullet\bullet}$) [81].

3.7. Modulus analysis

The experimental data can also be analysed within the framework of complex modulus. This formalism is required for minimizing the effects of electrode polarization and other interfacial phenomena of solid electrolytes [92]. The complex modulus can be calculated from the dielectric permittivity using the following expressions [93-96]:

$$\boldsymbol{M^*(\omega) = \frac{1}{\varepsilon^*(\omega)} = \frac{\varepsilon'(\omega)}{|\varepsilon^*(\omega)|^2} - j\frac{\varepsilon''(\omega)}{|\varepsilon^*(\omega)|^2} = M'(\omega) + jM''(\omega) = M_\infty \left[1 - \int_0^\infty e^{-i\omega t}\left(-\frac{d\Phi(t)}{dt}\right)dt\right]} \quad \textbf{(19)}$$

Where M' and M" represent the real and imaginary parts of the complex modulus M^*, $M_\infty = \frac{1}{\varepsilon_\infty}$ is the inverse of the high-frequency dielectric constant, and Φ(t) represents the Kohlrausch-Williams-Watts (KWW) electric relaxation function [96-98], which describes the deviation degree from the relaxation of a single charge carrier in the time domain:

$$\boldsymbol{\Phi(t) = e^{-\left(\frac{t}{\tau_{KWW}}\right)^{\beta_{KWW}}}} \quad \textbf{(20)}$$

Here, τ_{KWW} is the relaxation time and β_{Kww} is the parameter characterizing the deviation between the electric relaxation function of a real solid electrolyte and the Debye-type

relaxation function of an ideal solid electrolyte (0 <β <1). The function $\frac{d\Phi}{dt}$ can be approximated by various empirical functions such as Cole-Cole [99], Fuoss and Kirkwood [100], Cole and Davidson [101], Jonscher [102], or Havriliak and Negami [103]. Among these functions, Havriliak and Negami (HN) is the most used in the literature [104-106], given by the following expression [107]:

$$\varphi_{HN}(\omega) = \int_0^{\infty} e^{-i\omega t}\left(-\frac{d\Phi(t)}{dt}\right)dt = \frac{1}{[1+(j\omega\tau_{HN})^{\alpha}]^{\gamma}} \quad (21)$$

Where τ_{HN} represents the relaxation time, α and γ are shape parameters. These two shape parameters are related by the following formula [108, 109]:

$$\gamma = 1 - 0.812(1-\alpha)^{0.387} \quad (22)$$

According to the work of Alvarez et al. [108], the fitting parameters α and γ of the Havriliak-Negami function are related to the β_{KWW} parameter of the Kohlrausch-Williams-Watts empirical function by the following expression:

$$\beta_{KWW} = (\alpha\gamma)^{\frac{1}{1.123}} \quad (23)$$

The fitting parameters values are recorded in Table 6 and 7. Considering the Equation (19), the M' and M'' can be expressed as:

$$M' = M_{\infty}\left(1 - \frac{A}{A^2+B^2}\right) \quad (24)$$

and,

$$M'' = M_{\infty}\left(\frac{A}{A^2+B^2}\right) \quad (25)$$

Where;

$$A = 1 + (\omega\tau)^{\alpha}\cos\left(\frac{\alpha\pi}{2}\right) + \frac{1}{2}(\kappa-1)\,LnC\left[1 + (\omega\tau)^{\alpha}\cos\left(\frac{\alpha\pi}{2}\right)\right] + (\kappa - 1)\,(\omega\tau)^{\alpha}\,\psi\sin\left(\frac{\alpha\pi}{2}\right) \quad (26)$$

$$B = (\omega\tau)^{\alpha}\sin\left(\frac{\alpha\pi}{2}\right) + \frac{1}{2}(\kappa-1)\,LnC(\omega\tau)^{\alpha}\sin\left(\frac{\alpha\pi}{2}\right) - (\kappa-1)\left[1 + (\omega\tau)^{\alpha}\,\psi\cos\left(\frac{\alpha\pi}{2}\right)\right] \quad (27)$$

$$C = 1 + (\omega\tau)^{2\alpha} + (\omega\tau)^{2\alpha}\cos\left(\frac{\alpha\pi}{2}\right) \quad (28)$$

and,

$$\Psi = arctan\left[\frac{(\omega\tau)^{\alpha}\sin\left(\frac{\alpha\pi}{2}\right)}{1+(\omega\tau)^{\alpha}\cos\left(\frac{\alpha\pi}{2}\right)}\right] \quad (29)$$

Figure 16(a, b) and **Figure 17(a, b)** depicts the variation of the real and imaginary parts of the modulus as a function of frequency for different temperatures for our samples. The solid curves represent the calculated values of M' and M'' obtained from **Equations (20)** and **(21)**. The agreement between experimental and calculated curves shows that the adopted model accurately describes the material behavior. For each temperature and as the frequency increased, the imaginary part of the modulus continued rising, ultimately reaching a peak associated with relaxation M_{max}. This maximum corresponds to the characteristic frequency F_{max}. The domain corresponding to frequencies lower than F_{max} relates to long-distance movements of charge carriers, whereas the domain at frequencies higher than F_{max} corresponds to carriers more confined in their potential wells. Near the relaxation frequency F_{max}, there is a transition from long-distance to short-distance movement. In addition, the peaks' maxima shift towards higher frequencies with increasing temperature. At low frequencies, M' values are very low, indicating negligible electrode effects that can be ignored. At high frequencies, the M' curves reach a constant value equal to M_{∞}, attributed to relaxation processes. The relaxation time is estimated from the equation $2\pi F_m\tau_m=1$, with F_m being the relaxation frequency determined from the peak of the M'' frequency curve. The variation of the relaxation time with temperature can be described by the Arrhenius law:

$$\tau_m = \tau_0 e^{-\frac{E_{am}}{K_B T}} \quad (30)$$

Where E_{am} represents the activation energy. **Figure 18** illustrates the variation of $Ln(\tau_m)$ as a function of (1000/T) for the MNFO and MNFEuO samples. This variation follows the Arrhenius law. The deduced activation energies are summarized in **Table 3** and compared to those previously obtained from impedance and conductivity measurements. From this table, it is noteworthy that the activation energy values E, estimated from the modulus phenomenon, are of the same order of magnitude as those extracted from the peak of the Z'' curve and conductivity. These results once again justify the nature of electrical conduction in our samples, which is likely due to a hopping mechanism **[110-111]**.

3.8. Dielectric analysis

An analysis of the dielectric constant ε' and dielectric loss $Tan\varepsilon$ was performed for the MNFO and MNFEuO samples over a frequency range of 10^2 Hz to 10^7 Hz within a temperature spectrum of 380 K to 640 K. The ε' and $Tan\delta$ may be calculated using the following formulae:

$$\boldsymbol{\varepsilon' = \frac{Z''}{\omega C_0 (Z'^2 + Z''^2)}} \textbf{ (31)}$$

And,

$$\boldsymbol{Tan(\delta) = \frac{Z''}{Z'}} \textbf{ (32)}$$

Where $C_0 = \frac{\varepsilon_0 A}{e}$ denotes capacitance in farads of both samples and ε_0 is the permittivity of free space (approximately 8.854×10^{-12} F). For MNFO and MNFEuO compounds, the dielectric constant exhibits a higher value at lower frequencies, attributed to space charge polarization within the dielectric materials, as illustrated in **Figure 19(a, b)**. Conversely, the dielectric constant decreases with increasing frequency. At elevated frequencies, the ε' tends to saturate because the electrons can no longer respond adequately to the applied electric field, resulting in a phase lag in their directional alignment relative to the oscillating field **[112-113]**. This phenomenon can be elucidated through Maxwell–Wagner polarization theory and Koop's phenomenological theory **[114-115]**. According to this model, a dielectric medium is viewed as consisting of highly conductive grains that are more effective at lower frequencies, while poorly conducting grain boundaries become more significant at higher frequencies. The elevated value of ε′ at low frequencies is primarily due to interfacial polarization, where charge carriers accumulate at the grain boundaries **[116]**. At low frequencies, electron exchange between Fe^{2+} and Fe^{3+} takes place, leading to polarization in the samples. In contrast, at high frequencies, the electron exchange remains relatively unchanged with frequency, resulting in a stable behaviour.

Figure 20(a, b) illustrates the variation of tan(δ) as a function of both frequency and temperature for both ferrites. The behavior of Tan(δ) changes with these parameters, offering insights into the properties of the ferrite material. At lower frequencies, Tan(δ) values are higher, indicating that more resistive grain boundaries primarily contribute to energy dissipation in the ferrite. In contrast, at higher frequencies, the tangent loss

decreases, suggesting that less resistive grains become more influential in energy dissipation. Additionally, Tan(δ) increases with rising temperatures due to a thermally activated conduction process in the ferrite, where thermal energy boosts the material's conductivity, thereby increasing energy dissipation. Additionally, to elucidate the Eu^{3+} ions impact in the dielectric features of MNFO ferrite, **Figure 20(c)** shows a comparison of ε' and $Tan\delta$ for MNFO and MNFEuO at 560 K. As evident, the dielectric constant of MNFEuO is found to be superior to that of MNFO ferrite. Whereas the dielectric loss is found to be slightly lower to that of MNFO. In fact, the Eu^{3+} introduction into the Fe^{3+} site led to a conversion of some Fe^{2+} ions back to Fe^{3+} to maintain charge neutrality. This conversion may have enhanced the hopping between Fe^{3+} and Fe^{2+} ions and increased grain resistance, all of which contributed to the increase in ε′ of the material. Similar behaviour has been observed in Eu-doped $Co_{0.2}Zn_{0.3}Ni_{0.5}E_xFe_{2-x}O_4$ ferrites **[117]** and Eu-doped NiZnCo ferrites **[118]**, where the introduction of Eu^{3+} ions also enhance the dielectric properties in a comparable manner.

4. Conclusion

The successful synthesis of $Mg_{0.5}Ni_{0.5}Fe_2O_4$ (MNFO) and Eu-doped $Mg_{0.5}Ni_{0.5}Fe_{1.98}Eu_{0.02}O_4$ (MNFEuO) spinel ferrites via a solid-state method has been demonstrated through comprehensive structural, morphological, and dielectric analyses. XRD results confirmed the cubic structure, while SEM images revealed uniform, spherical particles. XPS analysis validated the elemental purity and oxidation states, further supporting the successful incorporation of Eu^{3+} ions. The Rietveld refinement analysis indicated an increase in lattice constant due to the larger ionic radius of Eu^{3+}, leading to enhanced dielectric properties. The superior dielectric and electrical characteristics of the Eu-doped ferrite underscore its potential for high-frequency applications and magnetodielectric devices. This study not only confirms the feasibility of using Eu-doped spinel ferrites in advanced technological applications but also provides a solid foundation for further research into rare-earth-doped ferrites, paving the way for their use in various industrial and technological fields. Although this study successfully demonstrates the synthesis and characterization of Eu-doped $Mg_{0.5}Ni_{0.5}Fe_2O_4$ spinel ferrites, limitations include the relatively low doping concentration and focus on dielectric properties alone. Future work could explore higher doping levels and a broader range of properties, including magnetic and impedance characteristics across a wider frequency spectrum. Additionally,

investigating the material's stability under varying environmental conditions and optimizing the synthesis method could enhance its practical applications. Exploring other rare-earth dopants or multi-doping strategies would also be valuable for tailoring ferrite properties for specific technological uses.

Author contributions

Souhir Bouzidi: investigation and conceptualization; **Najah Rhimi**: validation and writing – original draft; **Jamila Dhahri**: software and formal analysis; **Zouhaier Aloui**: formal analysis; **Abdelaziz Bouazizi**: supervision; **Kamel Khirouni**: software; **Malek Gassoumi**: supervision; and **Jean Juraszek:** investigation.

Research data policy and data availability statements

The datasets generated or analysed during the current study are available from the corresponding author on reasonable request.

Ethical approval

Not applicable

Declaration of interests

The authors declare that they have no known competing financial interests or personal relationships that could have appeared to influence the work reported in this paper.

Acknowledgment

The authors extend their appreciation to the Deanship of Research and Graduate Studies at King Khalid University for funding this work through Large Research Project under grant number RGP2/209/45.

References

[1] Y. Zhang, X. Xu, Machine learning band gaps of doped-TiO_2 photocatalysts from structural and morphological parameters, ACS omega, 5 (2020) 15344-15352.

[2] Y. Zhang, X. Xu, Predicting doped MgB_2 superconductor critical temperature from lattice parameters using Gaussian process regression, Physica C: Superconductivity and its applications, 573 (2020) 1353633.

[3] Y. Zhang, X. Xu, Predicting doped Fe-based superconductor critical temperature from structural and topological parameters using machine learning. International Journal of Materials Research, 112 (2021) 2-9.

[4] Y. Zhang, X. Xu, Machine learning f-doped Bi (Pb)–Sr–Ca–Cu–O superconducting transition temperature, Journal of Superconductivity and Novel Magnetism, 34 (2021) 63-73.

[5] X. Mao, Z. Li, M. Li, X. Xu, C. Yan, Z. Zhu, A. Du, Computational design and experimental validation of the optimal bimetal doped $SrCoO_{3-\delta}$ perovskite as solid oxide fuel cell cathode, J. Am. Chem. Soc. 143 (2021) 9507–9514.

[6] K. Ramam, S. Surabhi, S.C. Gurumurthy, M.P. Shilpa, K. Bindu, Ravikirana, S. Mundinamani, Dielectric and piezoelectric studies of dysprosium-doped BZT-BCNT perovskite ceramic system for sensors and actuator applications, J. Mater. Sci: Mater. Electron. 32 (2021) 18002–18011.

[7] M.R. Kannan, A. Logeswari, M.W. Carry, T. Vijayakumar, Synthesis and investigation of $(1–x)K_{0.5}Na_{0.5}NbO_3–(x)CaSnO_3$ lead free perovskite ceramics of high dielectric and piezoelectric properties for transducer applications, J. Mater. Sci: Mater. Electron. 33 (2022) 9224–9234.

[8] O. Amhoud, N. Zaim, M. Kerouad, A. Zaim, Effect of Cd^{2+} element substitution at the Nd^{3+} site on the magnetic, the magnetocaloric and hysteresis properties of $Nd_{1-x}Cd_xMnO_3$ perovskite: Monte Carlo study, Mater. Today. Proc. 45 (2021) 7531–7537.

[9] J. Boonlakhorn, P. Srepusharawoot, (Zn^{2+}+ Cd^{2+}) co-doped $CaCu_3Ti_4O_{12}$ ceramics with enhanced dielectric permittivity and reduced dielectric loss tangent, Materials Chemistry and Physics 314 (2024) 128941.

[10] J. Boonlakhorn, A. Changchuea, P. Suksangrat, P. Thongbai, P. Srepusharawoot, Significantly reduced the low-loss tangent in $A_{2/3}Cu_3Ti_4O_{12}$ (A= Gd and Sm) ceramics through a double-step calcination process, Journal of the European Ceramic Society, 44 (2024) 6390-6401.

[11] P. Suksangrat, J. Boonlakhorn, P. Srepusharawoot, $Y_{2/3-3/2}Sr$ $Cu_3Ti_4O_{12}$ polycrystalline ceramic: A structural and dielectric investigation, Ceramics International, 50 (2024) 30018-30029.

[12] J. Boonlakhorn, P. Suksangrat, P. Thongbai, P. Srepusharawoot, Dielectric Properties and Nonlinear Electrical Response of Nb^{5+}/Cr^{3+}-Codoped $CaCu_3Ti_4O_{12}$ Ceramics, ACS Applied Electronic Materials, 6 (2024) 2514-2524.

[13] J. Fan, L. Zhong, T. Yang, Z. Hu, High breakdown electric field and ultralow loss in Sb+ Ho co-doped TiO_2 giant dielectric ceramics induced by strongly coupled defect clusters, Journal of Materiomics (2024).

[14] A. Baykal, S. Guner, H. Gungunes, K.M. Batoo, Md. Amir, A. Manikandan, Journal of Inorganic and Organometallic Polymers and Materials, 28 (2018) 2533–2544]

[15] Y. Slimani, A. Baykal, Md. Amir, N. Tashkandi, H. Güngüneş, S. Guner, H.S. El Sayed, F. Aldakheel, T.A. Saleh, A. Manikandan, Ceramics International, 44 (2018) 15995-16004.

[16] U. A. Agú, M. I. Oliva, S. G. Marchetti, A. C. Heredia, S. G. Casuscelli, M. E. Crivello, Synthesis and characterization of a mixture of $CoFe_2O_4$ and $MgFe_2O_4$ from layered double hydroxides: Band gap energy and magnetic responses, Journal of magnetism and magnetic materials, 369 (2014) 249-259.

[17] A. M. Kumar, V. Ragavendran, J. Mayandi, K. Ramachandran, K. Jayakumar, Phase dependent electrochemical characteristics of bismuth ferrite: A bifunctional electrocatalyst for Supercapacitors and Dye-Sensitized Solar Cells. Colloids and Surfaces A: Physicochemical and Engineering Aspects, 656 (2023) 130529.

[18] J. Arul Hency Sheela, S. Lakshmanan, A. Manikandan, S. Arul Antony, Structural, Morphological and Optical Properties of ZnO, ZnO:Ni^{2+} and ZnO:Co^{2+} Nanostructures by Hydrothermal Process and Their Photocatalytic Activity, Journal of Inorganic and Organometallic Polymers and Materials 28 (2018) 2388–2398.

[19] M. Maria Lumina Sonia, S. Anand, V. Maria Vinosel, M. Asisi Janifer, S. Pauline, A. Manikandan, Effect of lattice strain on structure, morphology and magneto-dielectric

properties of spinel $NiGd_xFe_{2-x}O_4$ ferrite nano-crystallites synthesized by sol-gel route, Journal of Magnetism and Magnetic Materials, 466 (2018) 238-251.

[20] A.T. Ravichandran, J. Srinivas, A. Manikandan, A. Baykal, Enhanced Magneto-optical and Antibacterial Studies of $Bi_{1-x}Mg_xFeO_3$ ($0.0 \leq x \leq 0.15$)) Nanoparticles, Journal of Superconductivity and Novel Magnetism, 32 (2019) 1663–1670.

[21] M. G. Naseri, M.H.M. Ara, E.B. Saion, A.H. Shaari, Superparamagnetic magnesium ferrite nanoparticles fabricated by a simple, thermal-treatment method, J. Magn. Magn. Mater. 350 (2014) 141–147.

[22] M. Hashim, Alimuddin, S. Kumar, S.E. Shirsath, R.K. Kotnala, H. Chung, R. Kumar, Structural properties and magnetic interactions in $Ni_{0.5}Mg_{0.5}Fe_{2-x}Cr_xO_4$ ($0 \leq x \leq 1$) ferrite nanoparticles, Powder Technol. 229 (2012) 37-44.

[23] N. Hamdaoui, Y. Azizian-Kalandaragh, M. Khlifi, L. Beji, Structural, magnetic and dielectric properties of $Ni_{0.6}Mg_{0.4}Fe_2O_4$ ferromagnetic ferrite prepared by sol gel method, Ceram. Int. 45 (13) (2019) 16458-16465.

[24] H. Moradmard, S. Farjami Shayesteh, P. Tohidi, Z. Abbas, M. Khaleghi, Structural, magnetic and dielectric properties of magnesium doped nickel ferrite nanoparticles, J. Alloy. Comp. 650 (2015) 116-122.

[25] L. John Berchmans, R. Kalai Selvan, P.N. Selva Kumar, C.O. Augustin, Structural and electrical properties of $Ni_{1-x}Mg_xFe_2O_4$ synthesized by citrate gel process, J. Magn. Magn. Mater. 279 (2004) 103-110.

[26] M.A. Gabal, Y.M. Al Angari, H.M. Zaki, Structural, magnetic and electrical characterization of Mg–Ni nano-crystalline ferrites prepared through egg-white precursor, J. Magn. Magn. Mater. 363 (2014) 6-12.

[27] M.S. Sikder, M.D. Hossain, I. Sardar, Md. Sarowar Hossain, M.N.I. Khan, M.R. Rahman, Improved magnetic and dielectric quality factors with low losses in rare earth (Eu) substituted Co-Ni-Zn ferrites for high frequency devices, Results in Physics 46 (2023) 106320.

[28] I. Sardar, M. D. Hossain, M. S. Sikder, M.N.I. Khan, M.R. Rahman, Enhancement of coercivity, permeability, and dielectric properties of $Co_{0.2}Zn_{0.3}Ni_{0.5}Eu_xFe_{2-x}O_4$

ferrites for memory and high frequency devices, Journal of Rare Earths, 42 (2024) 1128-1135.

[29] J. Mahapatro, S. Agrawal, Effect of Eu^{3+} ions on electrical and dielectric properties of barium hexaferrites prepared by solution combustion method, Ceramics International 47 (2021) 20529-20543.

[30] S. Kumari, R. Rai, P. Kumar, P. Kumari, A. Dronov, Rietveld analysis and negative dielectric behavior of perovskite-like $La_{1-x}Eu_xMnO_3$ system, Ferroelectrics Letters Section 47 (2020) 61-70.

[31] P. Sivaprakash, S. Divya, S. Esakki Muthu, A. Ali, Z. Jaglicic, T. Hwan Oh, I. Kim, Materials Science and Engineering B 301 (2024) 117200.

[32] R.D. Shannon, Revised effective ionic radii and systematic studies of interatomic distances in halides and chalcogenides, Foundations of Crystallography, 32 (1976) 751-767.

[33] N. Rhimi, N. Dhahri, A. Dhahri, K. Dhahri, J. Dhahri, J. Juraszek, M. Hleili, N. Al-Harbi, B.M. Alotaibi, H.A. Alyousef, Cu^{2+} and W^{6+} co-doped $Na_{0.5}Bi_{0.5}TiO_3$ solid solution: An effective approach to inhibit oxygen vacancy generation and suppress oxygen ion conduction, Journal of Physics and Chemistry of Solids 192 (2024) 112102.

[34] R. Tholkappiyan, K. Vishista, Combustion synthesis of Mg–Er ferrite nanoparticles: cation distribution and structural, optical, and magnetic properties, Materials Science in Semiconductor Processing, 40 (2015) 631-642.

[35] J. George, K. E. Abraham, Gas sensing characteristics of magnesium ferrite and its doped variants. Physica B: Condensed Matter, 610 (2021) 412958.

[36] M.A. Gabal, R.M. El-Shishtawy, Y.M. Al Angari, Structural and magnetic properties of nano-crystalline Ni–Zn ferrites synthesized using egg-white precursor, J. Magn. Magn Mater. 324 (2012) 2258–2264.

[37] M. Imran Arshad, S. Arshad, K. Mahmood, Adnan Ali, N. Amin, Umaid-ur-Rehman, M. Isa, A. Akram, N. Sabir, M. Ajaz-un-Nabi, Impact of Mg doping on structural, spectral and dielectric properties of Cd–Cu nano ferrites prepared via sol-gel auto combustion method, Physica B: Condensed Matter 599 (2020) 412496.

[38] D.S. Mathew, R.S. Juang, An overview of the structure and magnetism of spinel ferrite nanoparticles and their synthesis in microemulsions, Chemical engineering journal, 129 (2007) 51-65.

[39] N. Rhimi, N. Dhahri, M. Khelifi, E.K. Hlil, J. Dhahri, Structural, morphological, optical and dielectric properties of sodium bismuth titanate ceramics, Inorganic Chemistry Communications, 146 (2022) 110119.

[40] S.B. Somvanshi, M.V. Khedkar, P.B. Kharat, K.M. Jadhav, Influential diamagnetic magnesium (Mg^{2+}) ion substitution in nano-spinel zinc ferrite ($ZnFe_2O4$): thermal, structural, spectral, optical and physisorption analysis, Ceramics International, 46 (2020) 8640-8650.

[41] J.A. Ascencio, Y. Mejia, H.B. Liu, C. Angeles, G. Canizal, Bioreduction synthesis of Eu− Au nanoparticles, Langmuir, 19 (2003) 5882-5886.

[42] C. Kittel, Introduction to Solid State Physics, seventh Ed.,Wiley, Singapore (1996).

[43] M.M. Haque, K.H. Maria, S. Choudhury, M.A. Bhuiyan, M.A. Hakim, Synthesis, microstructure and magnetic properties of Ni-Mg ferrites, J. Ceram. Process. Res, 14 (2013) 82-86.

[44] V.A. Bharati, S.B. Somvanshi, A.V. Humbe, V.D. Murumkar, V.V. Sondur, K.M, Jadhav, Influence of trivalent Al–Cr co-substitution on the structural, morphological and Mössbauer properties of nickel ferrite nanoparticles, Journal of Alloys and Compounds, 821 (2020) 153501.

[45] M.H. Ehsani, T. Raoufi, F.S. Razavi, Impact of Gd ion substitution on the magnetocaloric effect of $La_{0.6-x}Gd_xSr_{0.4}MnO_3$ (x= 0, 0.0125, 0.05, 0.10) manganites, J. Magn. Magn Mater. 475 (2019) 484–492.

[46] H.-S. Guo, L.-Z. Li, X.-H. Wu, Z.-C. Zhong, Z.-X. Tao, F.-H. Wang, T. Wang, Enhanced of the resonant frequency of NiZnCo ferrites induced by substitution of Fe ions with Gd ions, J. Magn. Magn Mater. 538 (2021) 168249.

[47] A. Kumar, N. Yadav, D.S. Rana, P. Kumar, M. Arora, R.P. Pant, Structural and magnetic studies of the nickel doped $CoFe_2O_4$ ferrite nanoparticles synthesized by the chemical co-precipitation method, J. Magn. Magn Mater. 394 (2015) 379-384.

[48] V.E. Basin, Advances in understanding the adhesion between solid substrates and organic coatings, Prog. Org. Coatings. 12 (1984) 213-250.

[49] R. Tholkappiyan, K. Vishista, Combustion synthesis of Mg–Er ferrite nanoparticles: cation distribution and structural, optical, and magnetic properties. Materials Science in Semiconductor Processing, 40 (2015) 631-642.

[50] X. Xu, T. Zhang, W. Wu, S. Jiang, J. Yang, Z. Liu, Optimizing the resistance of Ni-advanced weathering steel to marine atmospheric corrosion with the addition of Al or Mo, Construction and Building Materials, 279 (2021) 122341.

[51] N.V. Kosova, E.T. Devyatkina, V.V. Kaichev, Mixed layered Ni–Mn–Co hydroxides: Crystal structure, electronic state of ions, and thermal decomposition. Journal of Power Sources, 174 (2007) 735-740.

[52] C.P. Li, A. Proctor, D.M. Hercules, Curve Fitting Analysis of ESCA Ni 2p Spectra of Nickel-Oxygen Compounds and Ni/Al_2O_3 Catalysts, Appl. Spectr. 38 (1984) 880.

[53] A.F. Carley, S.D. Jackson, J.N. O'Shea, M.W. Roberts, The formation and characterisation of Ni^{3+}—an X-ray photoelectron spectroscopic investigation of potassium-doped Ni (110)–O, Surf. Sci. 440 (1999) L868-L874.

[54] C.S. Fadley, D.A. Shirley, Multiplet splitting of metal-atom electron binding energies, Phys. Rev. A2 (1970) 1109–1120.

[55] B. Wang, H. Chen, S. Wang, Y. Shi, X. Liu, Y. Fu, T. Liu, Construction of core-shell structured Co7Fe3@ C nanocapsules with strong wideband microwave absorption at ultra-thin thickness, Carbon, 184 (2021) 223-231.

[56] W. Ge, W. Gao, Y. Tian, P. Zhang, J. Zhu, Y. Li, Tunable dual-mode photoluminescences from $SrAl_2O_4$: Eu/Yb nanofibers by different atmospheric annealing, Journal of Alloys and Compounds 859 (2021) 158261.

[57] P. Kumar, M.C. Mathpal, G.K. Inwati, S. Kumar, M.M. Duvenhage, W.D. Roos, H.C. Swart, Study of defect-induced chemical modifications in spinel zinc-ferrites nanostructures by in-depth XPS investigation, Magnetochemistry, 9 (2023) 20.

[58] K. Kumari, R. Kumar, P.B. Barman, Magnetic field and temperature-dependent studies of structural and magnetic properties of $NiFe_2O_4$ films, Applied Physics A 126 (2020) 1-7.

[59] C. Tudisco, L. Pulvirenti, P. Cool, G.G. Condorelli, Porphyrin functionalized bismuth ferrite for enhanced solar light photocatalysis, Dalton Transactions 49 (2020) 8652-8660.

[60] V. Kassabova-Zhetcheva, Characterization of the citrate precursor, used for synthesis of nanosized Mg-Zn ferrites. Open Chemistry 7 (2009) 415-422.

[61] M. Wang, Y. Zhang, X. Liu, X. Wang, Crystallization mechanism and ac conductivity studies on strontium barium niobate glass–ceramics, J. Ceramics International, 39 (2013) 2069-2076.

[62] A. M. A. El Ata, M. K. El Nimr, S. M. Attia, D. El Kony, A. H. Al-Hammadi, Studies of AC electrical conductivity and initial magnetic permeability of rare-earth-substituted LiCo ferrites, J. Magn. Magn. Mater. 297 (2006) 33–43.

[63] A.R. Long, Frequency-dependent loss in amorphous semiconductors, Adv. Phys. 31 (1982) 553-637.

[64] M.A. Dar, K.M. Batoo, V. Verma, W.A. Siddiqui, R.K. Kotnala, Synthesis and characterization of nano-sized pure and Al-doped lithium ferrite having high value of dielectric constant, J. Alloys Compd. 493 (2010) 553–560.

[65] A.K. Jonscher, Analysis of the alternating current properties of ionic conductors, J. Mater. Sci, 13 (1978) 553.

[66] H.S. Mohanty, A. Kumar, B. Sahoo, P.K. Kurliya, D.K. Pradhan, Impedance spectroscopic study on microwave sintered $(1–x)Na_{0.5}Bi_{0.5}TiO_{3–x}BaTiO_3$ ceramics, J. Mater. Sci. Mater. Electron. 29 (2018) 6966–6977.

[67] M. Amara, J. Hellara, F. Bourguiba, J. Dhahri, A. Bchetnia, K. Taibi, E.K. Hlil, Structural, morphological, and dielectric properties of lead-free $BaFe_{1/2}Nb_{1/2}O_3$ based ceramics: toward a deeper understanding of the dielectric mechanisms, J. Mater. Sci. Mater. Electron. 33 (2022) 3485–3500.

[68] M. Chebbi, S. Mansouri, S. Hcini, N. Hamdaoui, L. El Mir, Study of sintering temperature effects on the structural and electrical properties of $Mg_{0.6}Co_{0.4}FeCrO_4$ ferrites synthesized by the sol–gel method. Journal of Inorganic and Organometallic Polymers and Materials, 33 (2023) 1201-1218.

[69] N. Rhimi, N. Dhahri, J. Laifi, F. Bourguiba, N. Abdelmoula, J. Dhahri, C. Castro, J. Juraszek, Deep insights into the Cu-and W-doped $Na_{0.5}Bi_{0.5}TiO_3$ solid solution: A study focusing on optical, dielectric and electrical properties, J. Mol. Struct. 1294 (2023) 136319.

[70] D. Harrabi, S. Hcini, J. Dhahri, N. Hamdaoui, R. Charguia, M.L. Bouazizi, S. Mansouri, Structural, Magnetic, and Dielectric Properties for $Mg_{0.6}Co_{0.2}Cu_{0.2}FeCrO_4$ Spinel Ferrites Prepared Under Different Calcination Temperatures. Journal of Superconductivity and Novel Magnetism, 36 (2023) 1549-1569.

[71] W. Jdey, T. Mzoughi, N. Hamdaoui, S. Hcini, S. Mansouri, Impact of the Calcination Temperature on Structural, Electrical and Dielectric Properties for $Mg_{0.6}Cu_{0.4}FeCrO_4$ Spinel Ferrites. Journal of Inorganic and Organometallic Polymers and Materials, 33 (2023) 3485-3500.

[72] R. Roy, A. Dutta, Structural, optical and enhanced electrical properties of vanadium alloyed sodium bismuth titanate solid solution synthesized by a chemical-mechanical hybrid method, J. Alloys Compd. 843 (2020) 155999.

[73] S. Bouzidi, N. Rhimi, A. Dhahri, A. Kallekh, Ch. Rayssi, F. Abdulaziz, A.H. Alsehli, M.M. Alsowayigh, Deep insights into morphological, structural and dielectric properties of $BaTi_{0.5}(Cr_{0.33}Mo_{0.17})O_3$ ceramics, Ceramics International 49 (2023) 39935–39944.

[74] K.D. Chandrasekhar, A.K. Das, C. Mitra, A. Venimadhav, The extrinsic origin of the magnetodielectric effect in the double perovskite La_2NiMnO_6, J. Phys. Condens. Matter 24 (2012) 495901.

[75] S.K. Deshpande, S.N. Achary, R. Mani, J. Gopalakrishnan, A.K. Tyagi, Low-temperature polaronic relaxations with variable range hopping conductivity in $FeTiMO_6$ (M=Ta,Nb,Sb), Phys. Rev. B 84 (2011) 064301.

[76] J. Liu, Q. Liu, W. Wang, Y. Liang, D. Lu, P. Zhu, Variable-range-hopping conduction and polaron dielectric relaxation in Cu and Nb co-doped $BaTiO_3$, J. Phys. Chem. Solid. 129 (2019) 111–121.

[77] F. Paquin, J. Rivnay, A. Salleo, N. Stingelin, C.S. Acuna, Multi-phase semicrystalline microstructures drive exciton dissociation in neat plastic semiconductors, J. Mater. Chem. C3 (2015)10715–10722.

[78] A. Lungu, I. Malaescu, C.N. Marin, P. Vlazan, P. Sfirloaga, The electrical properties of manganese ferrite powders prepared by two different methods. Physica B: Condensed Matter, 462 (2015) 80-85.

[79] C. Ang, J.R. Jurado, Z. Yu, M.T. Colomer, J.R. Frade, J.L. Baptista, Variable-range-hopping conduction and dielectric relaxation in disordered $Sr_{0.97}(Ti_{1-x}Fe_x)O_{3-\delta}$, Phys. Rev. B 57 (1998) 19.

[80] C.h. Rayssi, S. El.Kossi, J. Dhahri, K. Khirouni, Colossal dielectric constant and nondebye type relaxor in $Ca_{0.85}Er_{0.1}Ti_{1-x}Co_{4x/3}O_3$ (x=0.15 and 0.2) ceramic, J. Alloys Compd. 759 (2018) 93–99.

[81] C. Ang, Z. Yu, L. E. Cross, Oxygen-vacancy-related low-frequency dielectric relaxation and electrical conduction in Bi:$SrTiO_3$, Physical review B, 62 (2000) 228.

[82] J.R. Macdonad (Ed.), Impedance Spectroscopy, Wiley, New York, 1987.

[83] R. Pattanayak, S. Panigrahi, T. Dash, R. Muduli, D. Behera, Electric transport properties study of bulk $BaFe_{12}O_{19}$ by complex impedance spectroscopy, Physica B: Condensed Matter, 474 (2015) 57-63.

[84] D. Johnson, Zview program Version 2.1b, Scribner Associates (1990-1998).

[85] A. Omri, M. Bejar, E. Dhahri, M.A. Valente, M.P.F. Graca, L.C. Costa, Electrical conductivity and dielectric analysis of $La_{0.75}(Ca, Sr)_{0.25}Mn_{0.85}Ga_{0.15}O_3$ perovskite compound, Journal of Alloys and Compounds 536 (2012) 173-178.

[86] Y. Haittao, C. Sun, H. Hung, P. Hing, Single semicircular response of dielectric properties of diamond films, Thins Solid Films 381 (2001) 52.

[87] A. Huanosta, O. Alverz-Fregoso, E. Amano, C. Tabares-Munoz, M.E. Mendoza-Alverez et J.G. Mendoza-Alverez, AC impedance analysis on crystalline layered and polycrystalline bismuth titanate, J. Appl. phys. 69 (1991) 404.

[88] M. Ram, Role of grain boundary in transport properties of $LiCo_{3/5}Mn_{2/5}VO_4$ ceramics, Phys. B: Phys. Cond. Matter. 405 (2010) 602–605.

[89] M. L. Bouazizi, S. Hcini, K. Khirouni, F. Najar, A. H. Alshehri, Impact of calcination temperature on the structural, electrical, and dielectric properties of sol–gel synthesized $Ni_{0.6}Mg_{0.2}Co_{0.2}FeCrO_4$ spinel ferrites, Journal of Materials Science: Materials in Electronics 34 (2023) 1673.

[90] A.R. James, S. Priya, K. Uchino, K. Srinivas, V.V. Kiran, Investigation of Intrinsic Defect Structure in $0.91Pb(Zn_{1/3}Nb_{2/3})O_3–0.09PbTiO_3$ Single Crystal through AC Conductivity, J. Appl. Phys. 41 (2002) 5272-5276.

[91] M. Chebbi, S. Mansouri, S. Hcini, N. Hamdaoui, L. El Mir, Study of sintering temperature effects on the structural and electrical properties of $Mg_{0.6}Co_{0.4}FeCrO_4$ ferrites synthesized by the sol–gel method, Journal of Inorganic and Organometallic Polymers and Materials, 33 (2023) 1201-1218.

[92] J. Boonlakhorn, N. Chanlek, P. Thongbai, P. Srepusharawoot, Strongly enhanced dielectric response and structural investigation of (Sr^{2+}, Ge^{4+}) co-doped CCTO ceramics, The Journal of Physical Chemistry C, 124 (2020) 20682-20692.

[93] P.B. Macedo, C.T. Moynihan, R. Bose, The role of ionic diffusion in polarisation in vitreous ionic conductors, Phys. Chem. Glasses. 13 (1972) 171.

[94] M. Ganguly, M. Harish Bhat, K.J. Rao, Lithium-ion transport in $Li_2SO_4–Li_2O–B_2O_3$ glasses, Phys. Chem. Glasses. 40 (1999) 297.

[95] S. Lanfredi, P.S. Saia, R. Lebullenger, A.C. Hernandes, Electric conductivity and relaxation in fluoride, fluorophosphate and phosphate glasses: analysis by impedance spectroscopy, Solid. State. Ionics, 146 (2002) 329.

[96] S. Ghosh, A. Ghosh, Electrical conductivity and conductivity relaxation in mixed alkali fluoride glasses, Solid. Stat. Ionics. 149 (2002) 67.

[97] D.C. Sinclair, A.R. West, Impedance and modulus spectroscopy of semiconducting $BaTiO_3$ showing positive temperature coefficient of resistance, J. Appl. Phys. 66 (1989) 3850.

[98] R. Kohlrausch. Prog. Ann. 123 (1847) 393.

[99] K.S. Cole, R.H. Cole, Dispersion and absorption in dielectrics I. Alternating current characteristics, J. Chem. Phys. 9 (1941) 341.

[100] R.M. Fuoss, J.G. Kirkwood, Electrical Properties of Solids. VIII. Dipole Moments in Polyvinyl Chloride-Diphenyl Systems, J. Am. Chem. Soc. 63 (1941) 385.

[101] D.W. Davidson, R.H. Cole, Dielectric Relaxation in Glycerol, Propylene Glycol, and n-Propanol, J. Chem. Phys. 19 (1951) 1484.

[102] A.K. Jonscher, A new model of dielectric loss in polymers, Colloid. Polym. Sci 253 (1975) 231.

[103] S. Havriliak, S.Negami, A complex plane representation of dielectric and mechanical relaxation processes in some polymers, Polymer. 8 (1967) 161.

[104] M.C. Ediger, C.A. Angell, S.R. Nagel, Supercooled liquids and glasses, J. Phys. Chem. 100 (1996) 13200.

[105] C.A. Angell, Proc. Natl. Acad. Sci. USA. 92 (1995) 6675.

[106] C.J.F. Bottcher, Elsevier, Amsterdam, 1 (1973) 36.

[107] G. Williams, D.C. Watts, Trans. Faraday Soc. 66 (1990) 2727.

[108] F. Alvarez, A. Algeria, J. Colmenero, Relationship between the time-domain Kohlrausch-Williams-Watts and frequency-domain Havriliak - Negami relaxation functions, J. Phys. Rev. B 44 (1991) 7306.

[109] A. Algeria, E. Echevarria, L. Goiyiandia, I. Telleria, alpha.-Relaxation in the Glass Transition Range of Amorphous Polymers. 1. Temperature Behavior across the Glass transition, J. Colmenero, Macromolecules. 28 (1995) 1516.

[110] S-P. Szu, C-Y. Lin, AC impedance studies of copper doped silica glass, Mat. Chem. Phys. 82 (2003) 295.

[111] P. Dhak, D. Dhak, M. Das, K. Pramanik, Impedance spectroscopy study of $LaMnO_3$ modified $BaTiO_3$ ceramics, Mater. Sci. Eng B. 164 (2009) 165.

[112] K. Mohit, S.K. Rout, S. Parida, G.P. Singh, S.K. Sharma, S.K. Pradhan, I.W. Kim, Structural, optical and dielectric studies of $Ni_xZn_{1-x}Fe_2O_4$ prepared by auto combustion route, J. Phys. B 407 (2012) 935–942.

[113] D. Narsimulu, B. Nageswara Rao, M. Venkateswarlu, E.S. Srinadhu, N. Satyanarayana, Electrical and electrochemical studies of nanocrystalline mesoporous

$MgFe_2O_4$ as anode material for lithium battery applications, J. Ceram. Int. 45 (2016) 16789–16797.

[114] A. Kumari, S. Sanghi, A. Agarwal, O. Singh, Investigation of crystal structure, dielectric properties, impedance spectroscopy and magnetic properties of $(1–x)BaTiO_3–(x)Ba_{0.9}Ca_{0.1}Fe_{12}O_{19}$ multiferroic composites, Ceram. Int. 47 (2021) 23088-23100.

[115] C.G. Koops, On the dispersion of resistivity and dielectric constant of some semiconductors at audio frequencies, Phys. Rev. 83 (1951) 121-124.

[116] Z. Xu, H. Qiang, Y. Chen, Z. Chen, Microstructure and enhanced dielectric properties of yttrium and zirconium co-doped $CaCu_3Ti_4O_{12}$ ceramics, Mater. Chem. Phys. 191 (2017) 1-5.

[117] I. Sardar, M.D. Hossain, M.S. Sikder, M.N.I. Khan, M.R. Rahman, Enhancement of coercivity, permeability, and dielectric properties of $Co_{0.2}Zn_{0.3}Ni_{0.5}EuxFe_{2–x}O_4$ ferrites for memory and high frequency devices, Journal of Rare Earths, 42 (2024) 1128-1135.

[118] Y. Jiao, X. Zhang, Y.-L. Li, S.-J. Huang, B.-J. Wang, R.-D. Mao, L.-Z. Li, J. Tang, X.-H. Wu, Study on the high resistivity and resonant frequency characteristics of Eu-doped NiZnCo ferrites. Ceramics International, 50(2024). (19), 36811-36819.

Tables list:

Figures List

Figure 18: The variation of Ln(τ_m) as a function of (1000/T) for the MNFO and MNFEuO samples.

Figure 19: Variation of the dielectric constant ε' as a function of frequency for different temperatures for the MNFO and MNFEuO samples.

Figure 20: (a, b) Variation of the dielectric loss $Tan\delta$ as a function of frequency for different temperatures for the MNFO and MNFEuO samples. **(c)** A comparison of ε' and $Tan\delta$ for MNFO and MNFEuO at 560 K.

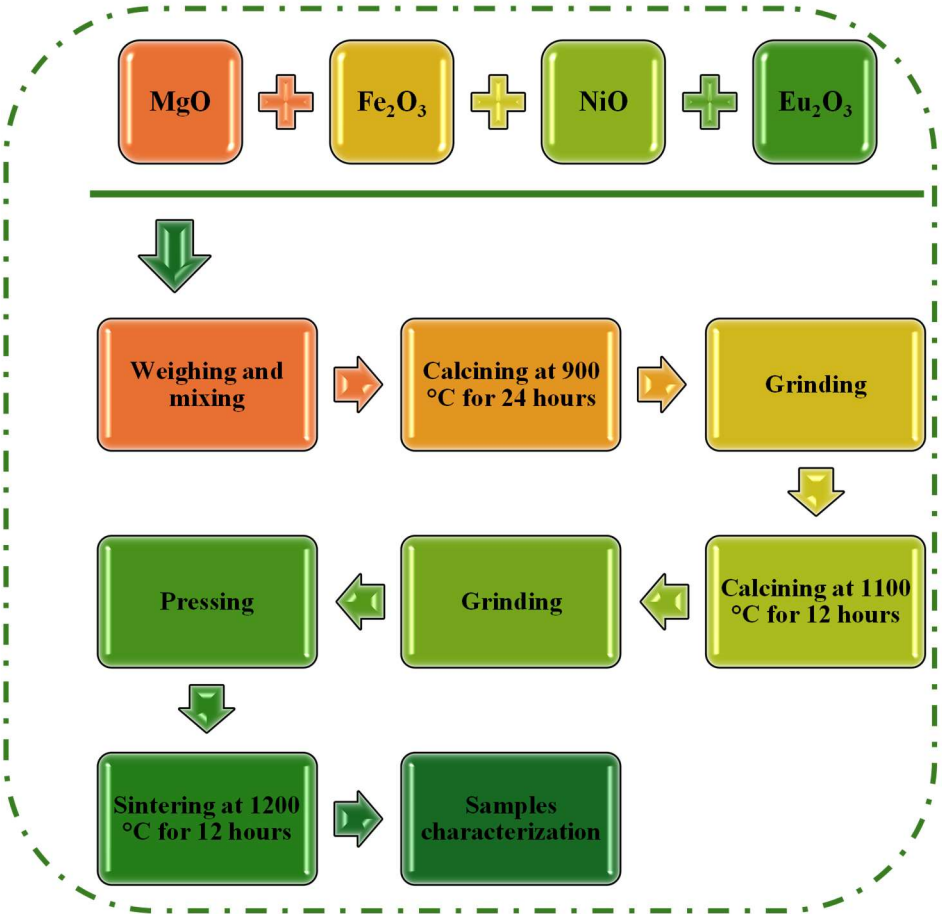
MgO
Fe_2O_3
NiO
Eu_2O_3
Weighing and mixing
Calcining at 900 °C for 24 hours
Grinding
Calcining at 1100 °C for 12 hours
Grinding
Pressing
Sintering at 1200 °C for 12 hours
Samples characterization

Figure 1

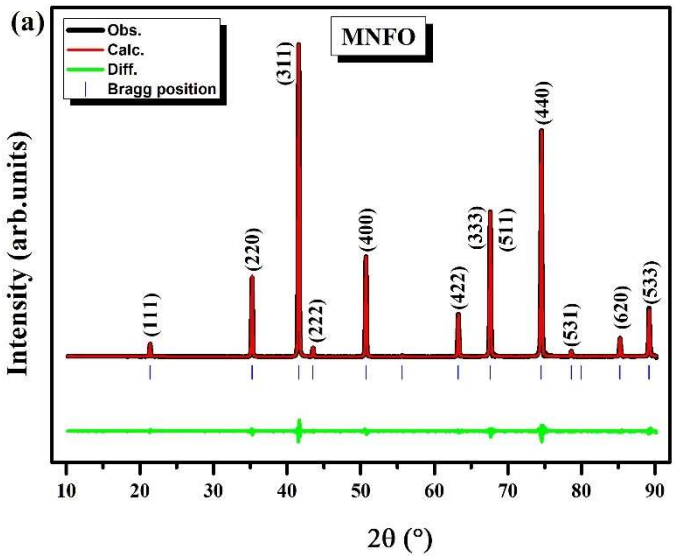
(a)
Obs.
Calc.
Diff.
Bragg position
MNFO
(311)
(220)
(400)
(222)
(422)
(333)
(511)
(440)
(111)
(531)
(620)
(533)
Intensity (arb.units)
10
20
30
40
50
60
70
80
90
2θ (°)

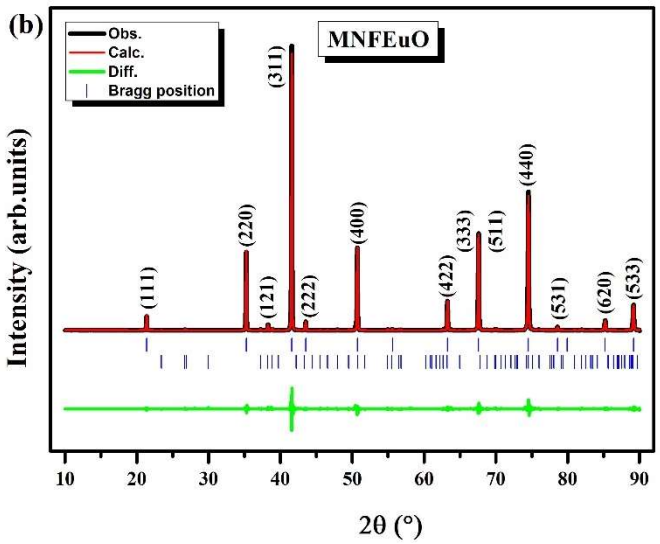
(b)
Obs.
Calc.
Diff.
Bragg position
MNFEuO
(311)
(220)
(121)
(400)
(222)
(422)
(333)
(511)
(440)
(111)
(531)
(620)
(533)
Intensity (arb.units)
10
20
30
40
50
60
70
80
90
2θ (°)

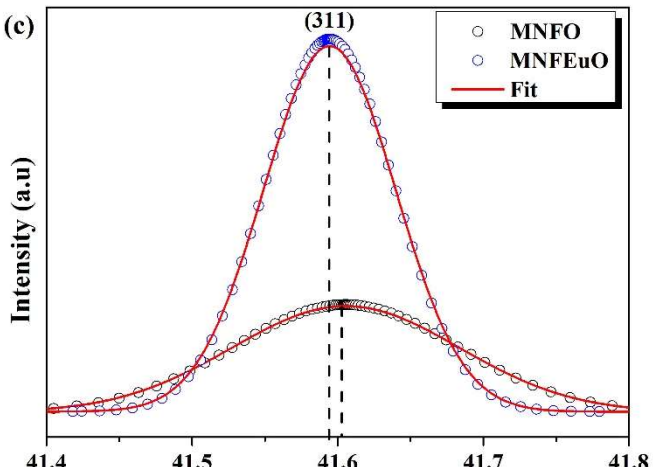
(c)
(311)
MNFO
MNFEuO
Fit
Intensity (a.u)
41.4
41.5
41.6
41.7
41.8

Figure 2

Table 1

Sample	MNFO	MNFEuO
Crystal system	Cubic	
Space group	$Fd\bar{3}m$	
Lattice parameters		
a(Å)	8.353	8.355
b(Å)	8.353	8.355
c(Å)	8.353	8.355
Cell volume V(Å^3)	582.904	583.348
Tetrahedral site (Mg1/Ni/Fe1)		
x	0.12500	0.12500
y	0.12500	0.12500
z	0.12500	0.12500
Octahedral site (Mg2/Fe2/Eu)		
x	0.50000	0.50000
y	0.50000	0.50000
z	0.50000	0.50000
O		
x	0.25379	0.25213
y	0.25379	0.25213
z	0.25379	0.25213
R-factors		
R_p (%)	4.97	7.97
R_{wp} (%)	8.53	9.50
R_{exp} (%)	3.42	2.42
χ^2	5.21	5.80
Crystallite size	46	80

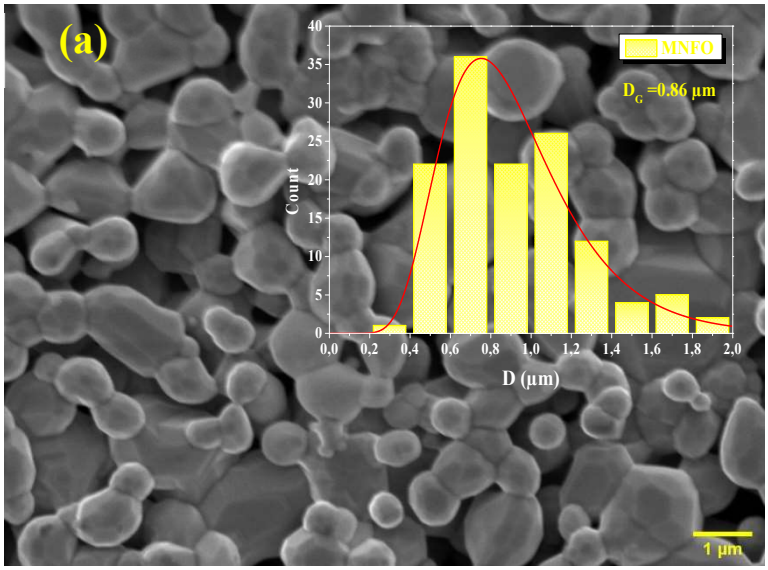
(a)
MNFO
D_G =0.86 µm
Count
D (µm)
1 µm

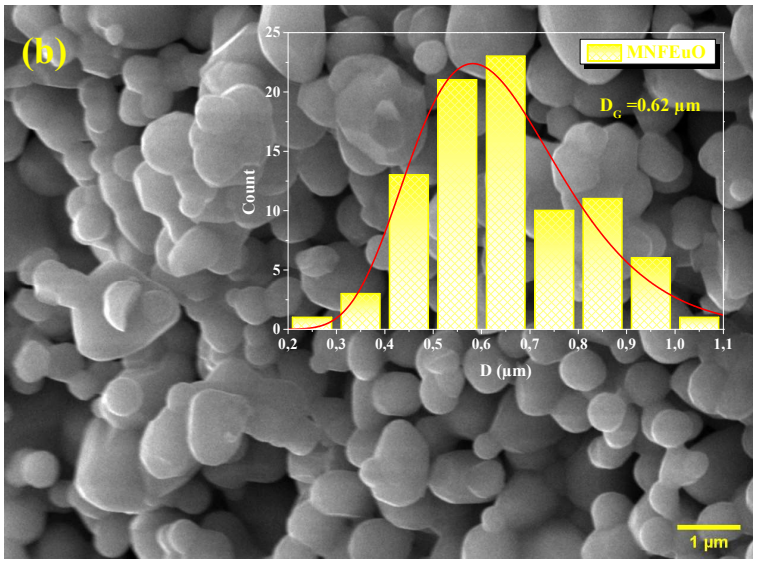
(b)
MNFEuO
D_G =0.62 µm
Count
D (µm)
1 µm

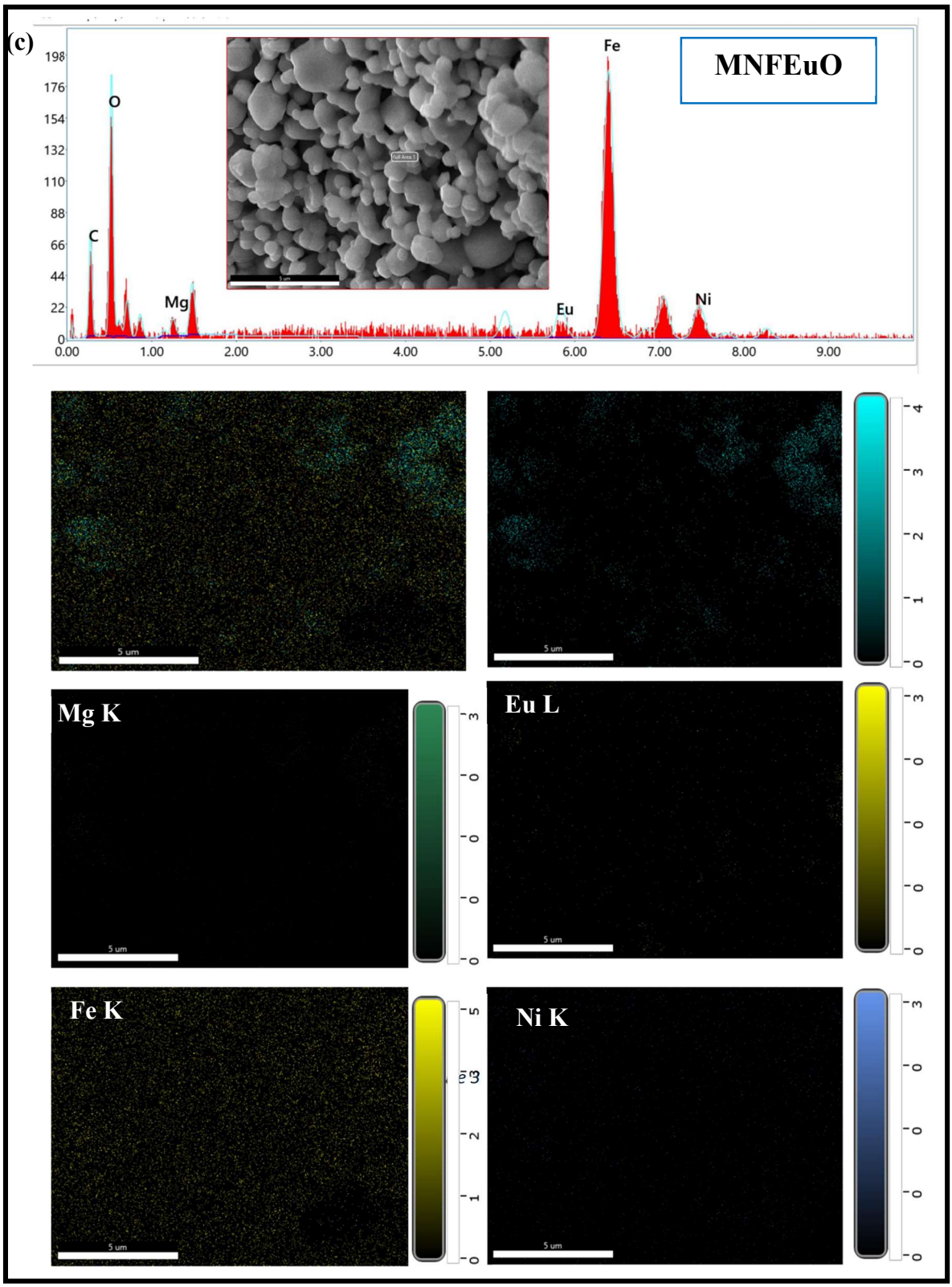
(c)
MNFEuO
O
C
Mg
Eu
Fe
Ni
0.00
1.00
2.00
3.00
4.00
5.00
6.00
7.00
8.00
9.00
Mg K
Eu L
Fe K
Ni K
5 um

Figure 3

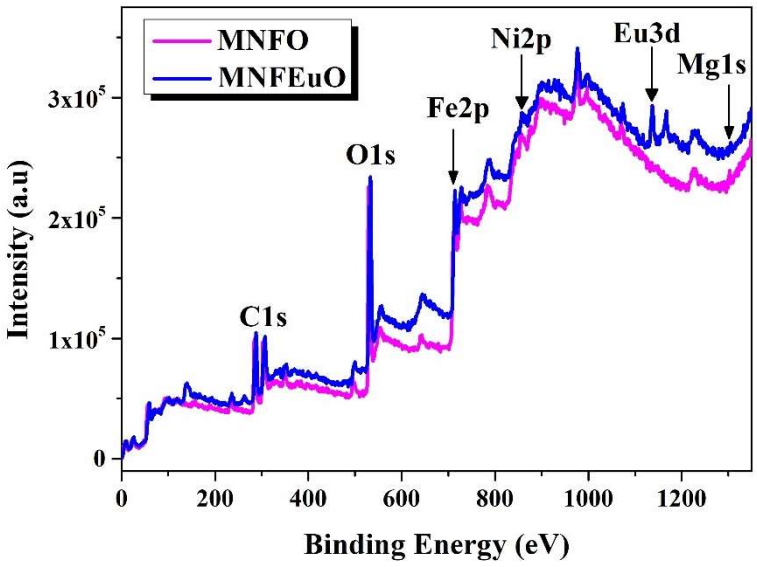
MNFO
MNFEuO
Ni2p
Eu3d
Mg1s
Fe2p
O1s
C1s
Intensity (a.u)
3x10^5
2x10^5
1x10^5
0
0
200
400
600
800
1000
1200
Binding Energy (eV)

Figure 4

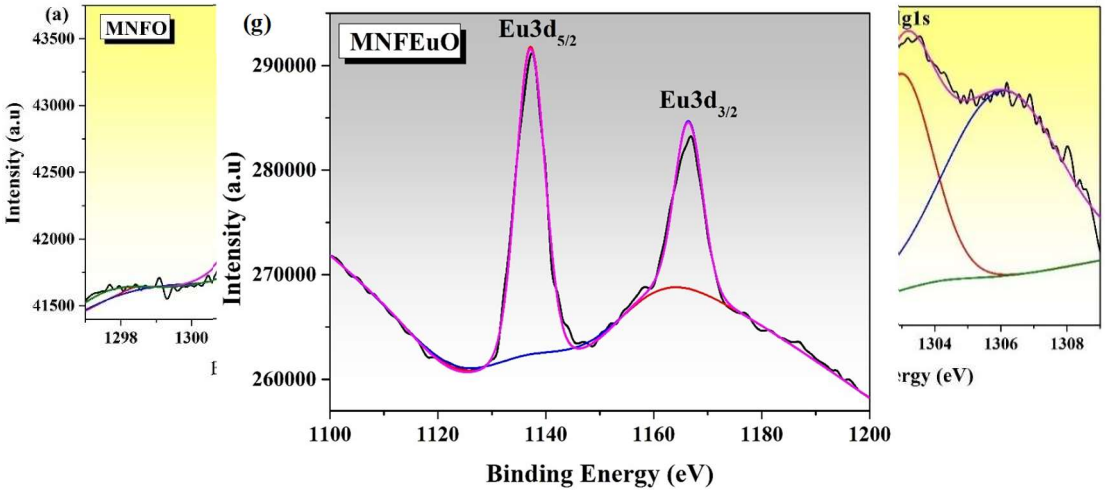
(a)
MNFO
Intensity (a.u)
(g)
MNFEuO
Eu3d5/2
Eu3d3/2
Intensity (a.u)
Binding Energy (eV)
g1s
rgy (eV)

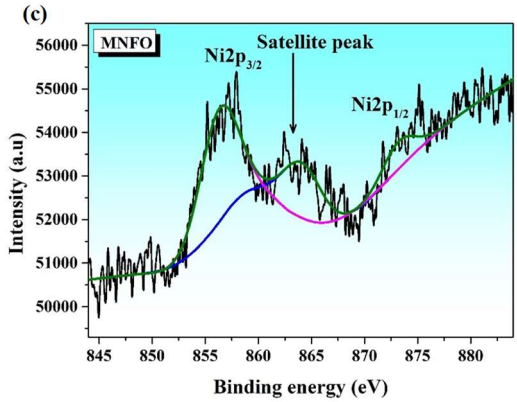
(c)
MNFO
Satellite peak
Ni2p3/2
Ni2p1/2
Intensity (a.u)
Binding energy (eV)

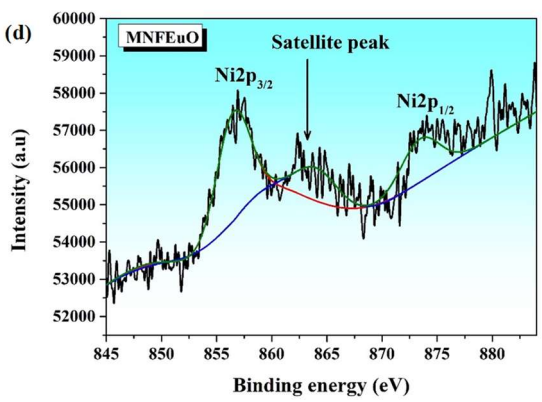
(d)
MNFEuO
Satellite peak
Ni2p3/2
Ni2p1/2
Intensity (a.u)
Binding energy (eV)

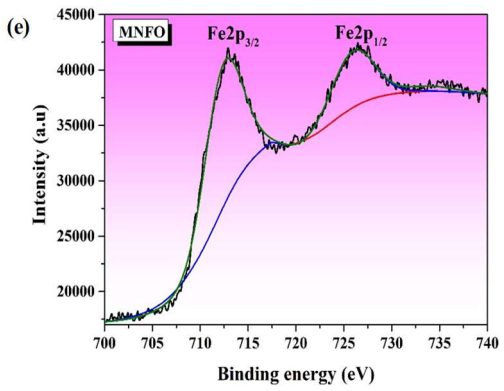
(e)
MNFO
Fe2p3/2
Fe2p1/2
Intensity (a.u)
Binding energy (eV)

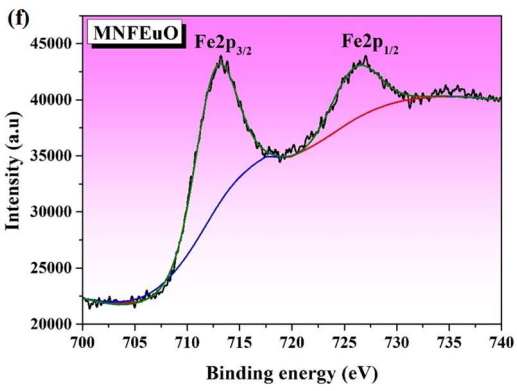
(f)
MNFEuO
Fe2p3/2
Fe2p1/2
Intensity (a.u)
Binding energy (eV)

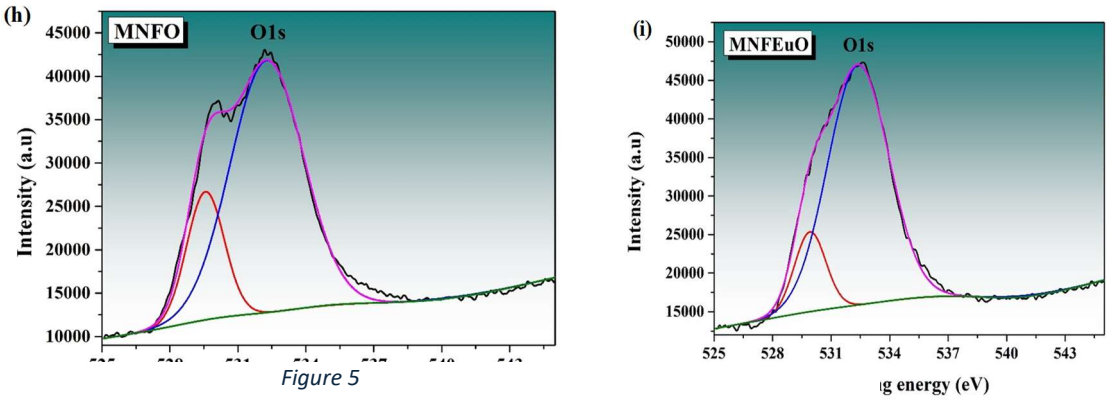
(h)
MNFO
O1s
Intensity (a.u)
45000
40000
35000
30000
25000
20000
15000
10000
(i)
MNFEuO
O1s
Intensity (a.u)
50000
45000
40000
35000
30000
25000
20000
15000
525
528
531
534
537
540
543
g energy (eV)

Figure 5

Table 2

Sample	Core level	Binding Energy (eV)	FWHM	Oxidation state
MNFO	Mg1s	1303.21	2.61	2+
		1305.74	3.49	2+
	$Ni2p_{3/2}$	856.31	4.25	2+
	$Ni2p_{1/2}$	873.19	3.55	2+
	$Fe2p_{3/2}$	712.33	4.45	3+
	$Fe2p_{1/2}$	725.94	5.19	2+
	O1s	529.57	1.95	2-
		532.28	3.79	2-
MNFEuO	Mg1s	1302.95	2.30	2+
		1306.04	4.07	2+
	$Ni2p_{3/2}$	856.50	3.57	2+
	$Ni2p_{1/2}$	873.43	4.10	2+
	$Fe2p_{3/2}$	712.64	4.48	3+
	$Fe2p_{1/2}$	726.06	5.19	2+
	O1s	529.92	1.90	2-
		532.39	3.68	2-
	$Eu3d_{3/2}$	1166.44	6.04	3+
	$Eu3d_{5/2}$	1137.15	6.26	3+

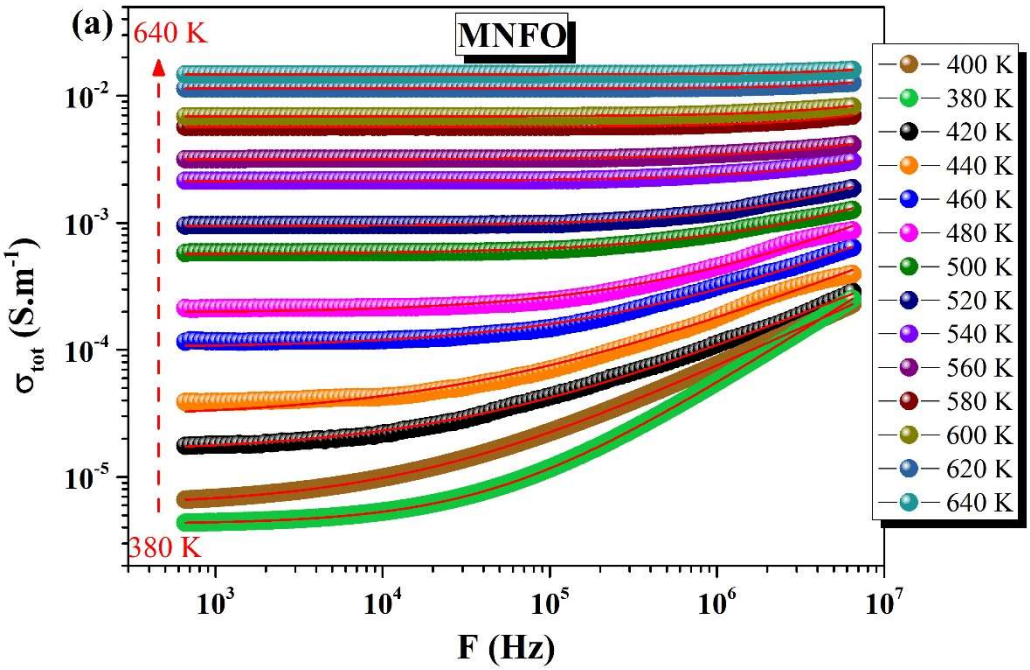
(a)
MNFO
640 K
380 K
400 K
380 K
420 K
440 K
460 K
480 K
500 K
520 K
540 K
560 K
580 K
600 K
620 K
640 K
σ_{tot} (S.m^{-1})
F (Hz)

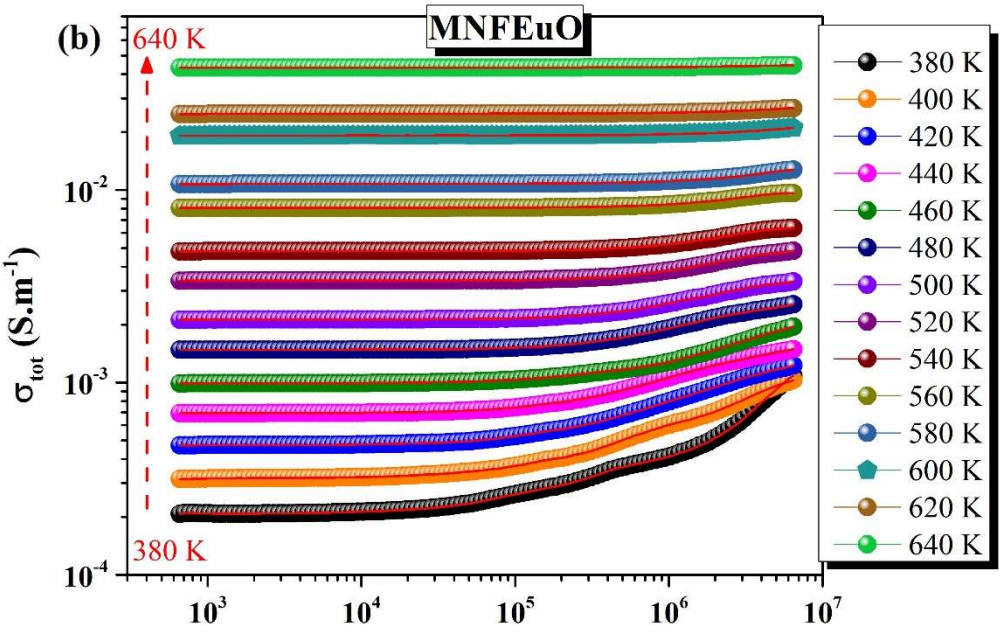
(b)
MNFEuO
640 K
380 K
380 K
400 K
420 K
440 K
460 K
480 K
500 K
520 K
540 K
560 K
580 K
600 K
620 K
640 K
σ_{tot} (S.m^{-1})

Figure 6

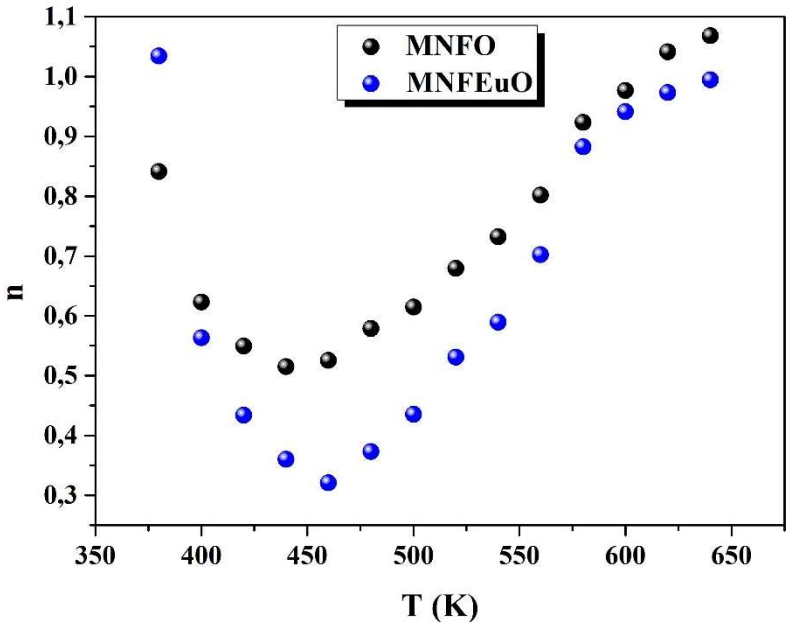
MNFO
MNFEuO
n
T (K)
1,1
1,0
0,9
0,8
0,7
0,6
0,5
0,4
0,3
350
400
450
500
550
600
650

Figure 7

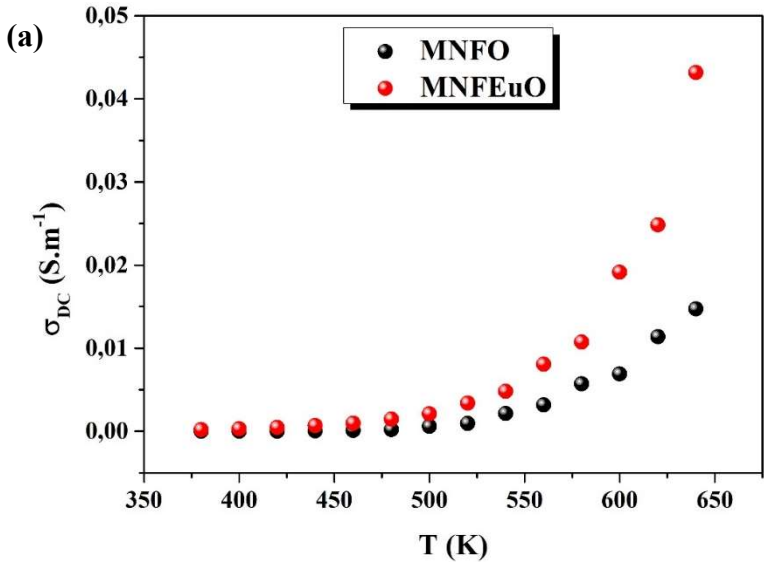
(a)
MNFO
MNFEuO
0,05
0,04
0,03
0,02
0,01
0,00
σDC (S.m-1)
350
400
450
500
550
600
650
T (K)

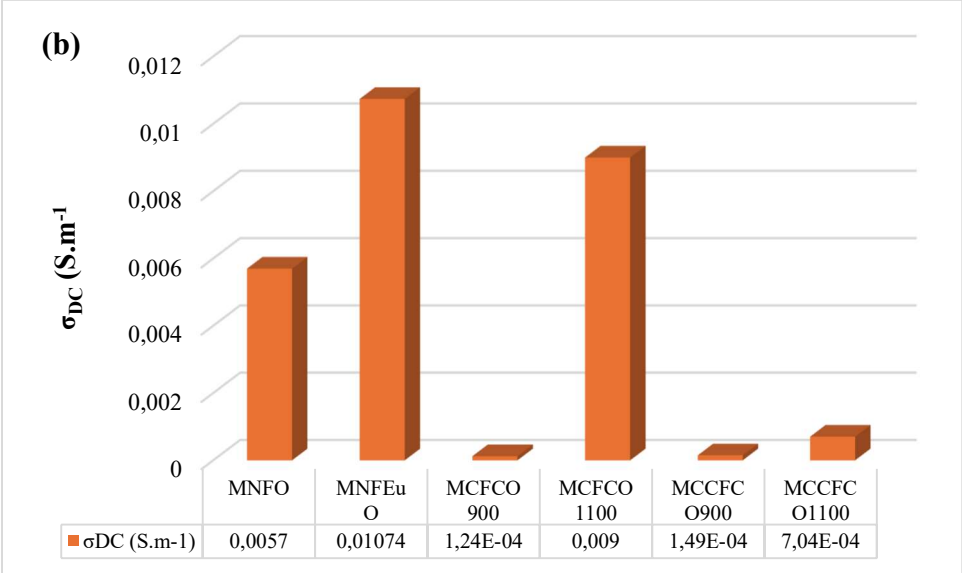
(b)
0,012
0,01
0,008
0,006
0,004
0,002
0
σDC (S.m-1)
MNFO
MNFEuO
MCFCO 900
MCFCO 1100
MCCFCO900
MCCFCO1100
σDC (S.m-1)
0,0057
0,01074
1,24E-04
0,009
1,49E-04
7,04E-04

Figure 8

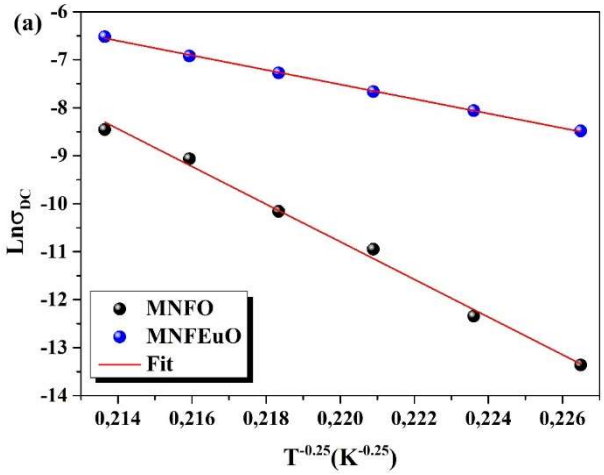
(a)
-6
-7
-8
-9
-10
-11
-12
-13
-14
Lnσ_DC
MNFO
MNFEuO
Fit
0,214
0,216
0,218
0,220
0,222
0,224
0,226
T^-0.25(K^-0.25)

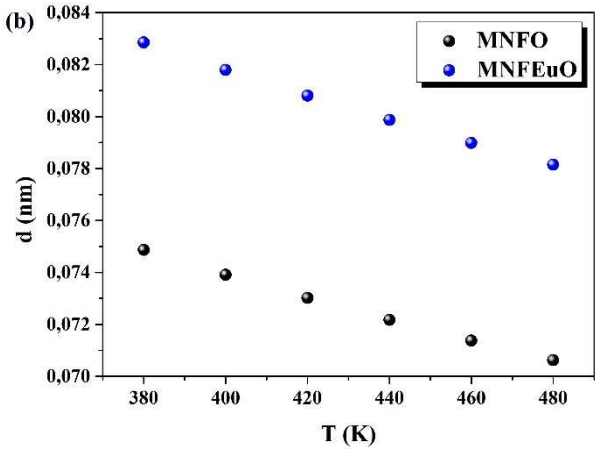
(b)
0,084
0,082
0,080
0,078
0,076
0,074
0,072
0,070
d (nm)
MNFO
MNFEuO
380
400
420
440
460
480
T (K)

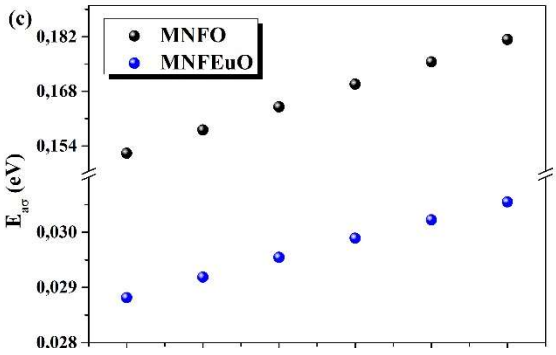
(c)
0,182
0,168
0,154
0,030
0,029
0,028
E_act (eV)
MNFO
MNFEuO

Figure 9

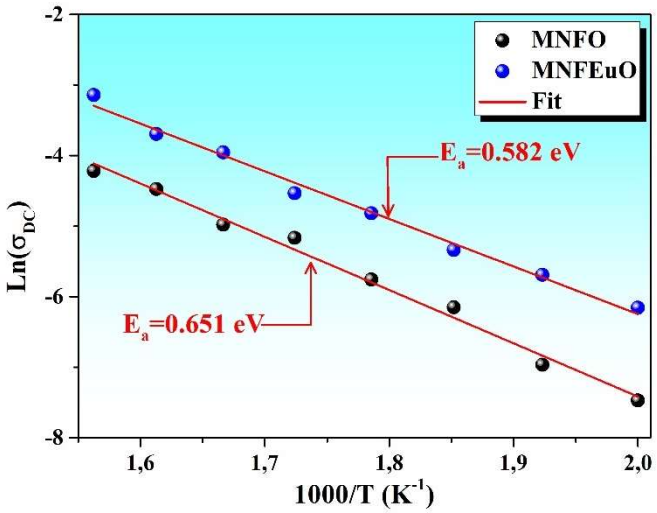

Figure 10

Table 3

Sample		MNFO	MNFEuO
From conductivity	Region I	0.15-0.18	0.028-0.030
	Region II	0.651	0.582
From Impedance		0.725	0.721
From Modulus		0.693	0.717

Table 4

Sample	MNFO	MNFEuO	$MnFe_2O_4$
Ref.	This work	This work	[56]
Synthesis method	Solid-state	Solid-state	Co-precipitation
ρ_{EF} (10^{17} eV^{-1} cm^{-3})	3.74×10^{-2}	1.77	0.788
T0 (10^8 K)	237	5	24.4

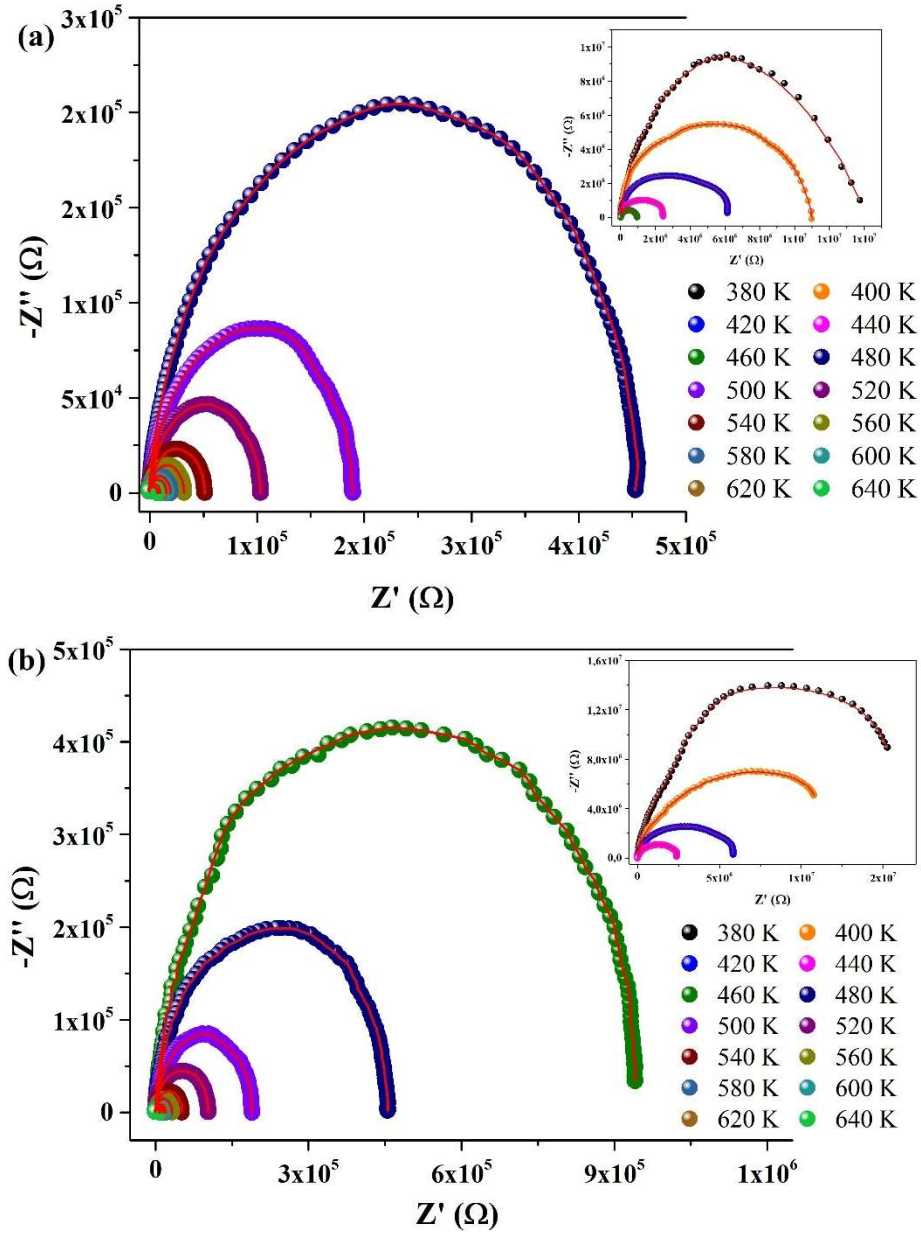
(a)
-Z'' (Ω)
Z' (Ω)
380 K
400 K
420 K
440 K
460 K
480 K
500 K
520 K
540 K
560 K
580 K
600 K
620 K
640 K
(b)
-Z'' (Ω)
Z' (Ω)
380 K
400 K
420 K
440 K
460 K
480 K
500 K
520 K
540 K
560 K
580 K
600 K
620 K
640 K

Figure 11

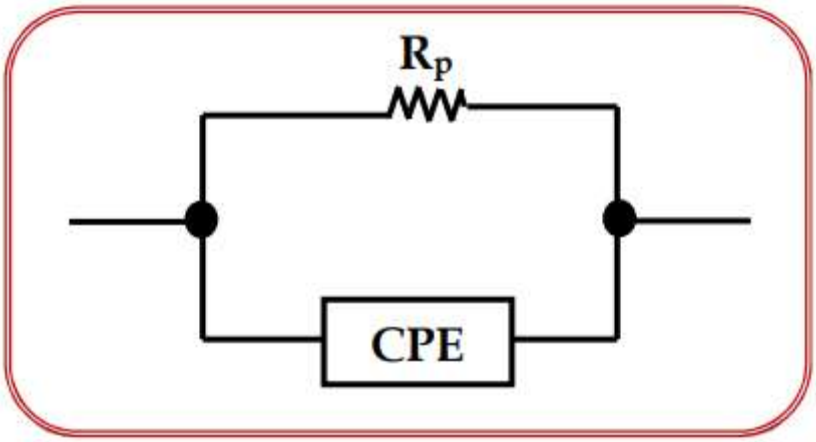

Figure 12

Table 5

Sample		MNFO			MNFEuO	
T (K)	**R_p (Ω)**	**CPE-T (nF)**	**CPE-P**	**R_p (Ω)**	**CPE-T (nF)**	**CPE-P**
380	6872	114.01	0.778	9178	201.32	0.773
400	6381	130.36	0.760	8997	209.81	0.853
420	5466	139.59	0.751	7347	245.78	0.891
440	4536	144.37	0.750	6730	260.42	0.905
460	3459	152.41	0.763	5137	262.13	0.918
480	2706	177.81	0.742	4393	269.42	0.893
500	1825.1	196.53	0.612	3063	273.06	0.886
520	1593	224.90	0.732	2017	279.19	0.877
540	1163	239.39	0.734	1732	287.82	0.862
560	890.8	260.75	0.728	1570	293.97	0.850
580	812.3	274.76	0.720	1491	309.20	0.857
600	504.3	278.34	0.742	988	310.79	0.833
620	321	305.00	0.601	643	313.14	0.877
640	271	314.23	0.564	422	326.74	0.901

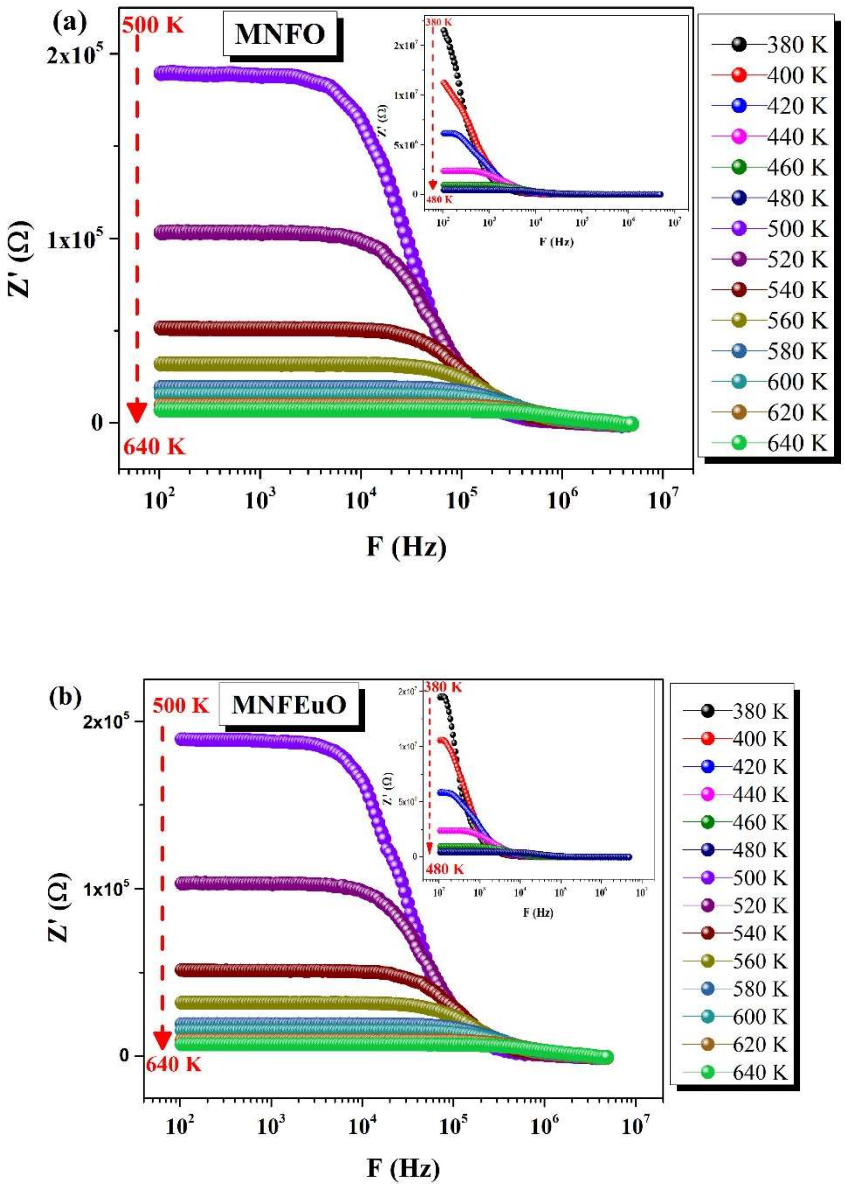
(a)
500 K
MNFO
2x10^5
1x10^5
0
640 K
Z' (Ω)
F (Hz)
380 K
480 K
380 K
400 K
420 K
440 K
460 K
480 K
500 K
520 K
540 K
560 K
580 K
600 K
620 K
640 K
(b)
500 K
MNFEuO
2x10^5
1x10^5
0
640 K
Z' (Ω)
F (Hz)
380 K
480 K
380 K
400 K
420 K
440 K
460 K
480 K
500 K
520 K
540 K
560 K
580 K
600 K
620 K
640 K

Figure 13

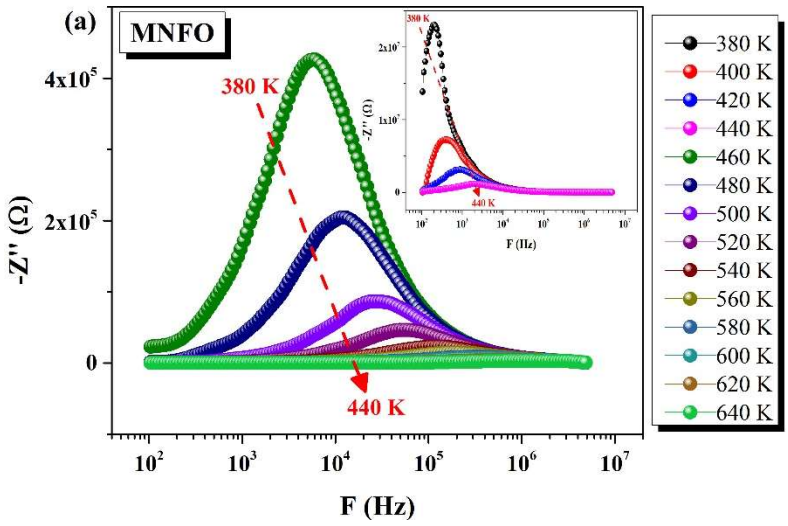
(a)
MNFO
380 K
440 K
-Z'' (Ω)
F (Hz)
380 K
400 K
420 K
440 K
460 K
480 K
500 K
520 K
540 K
560 K
580 K
600 K
620 K
640 K

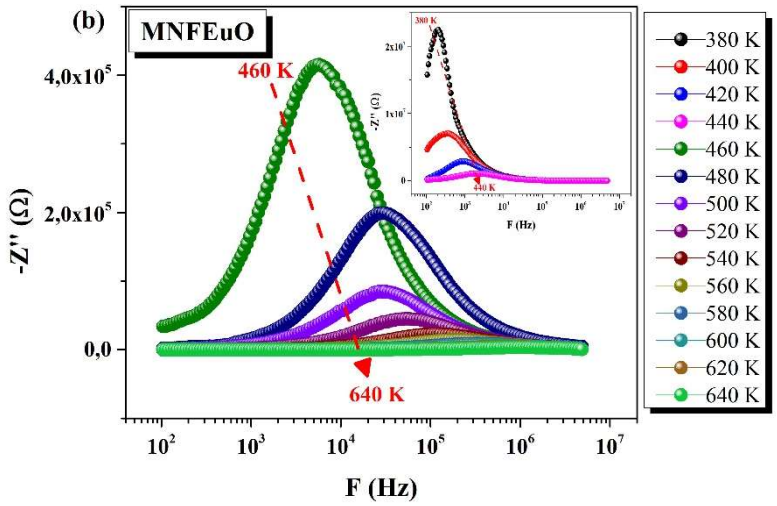
(b)
MNFEuO
460 K
640 K
-Z'' (Ω)
F (Hz)
380 K
400 K
420 K
440 K
460 K
480 K
500 K
520 K
540 K
560 K
580 K
600 K
620 K
640 K

Figure 14

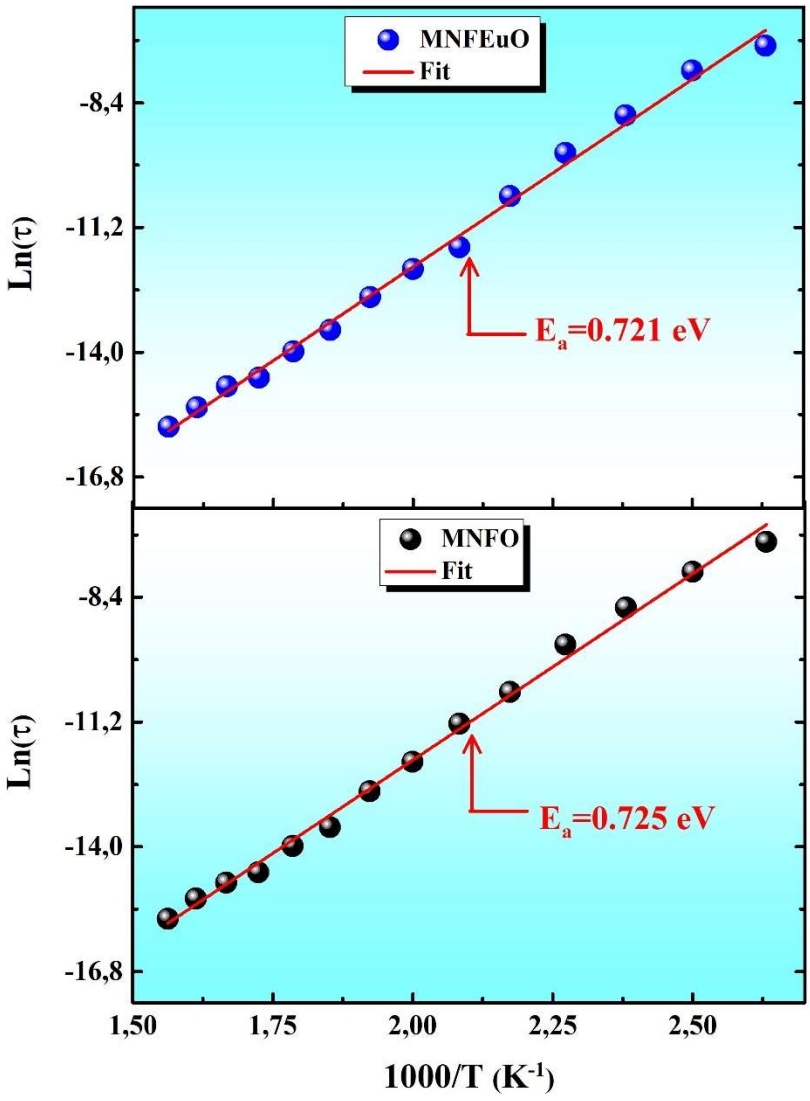
MNFEuO
Fit
E_a=0.721 eV
MNFO
Fit
E_a=0.725 eV
Ln(τ)
-8,4
-11,2
-14,0
-16,8
1,50
1,75
2,00
2,25
2,50
1000/T (K^-1)

Figure 15

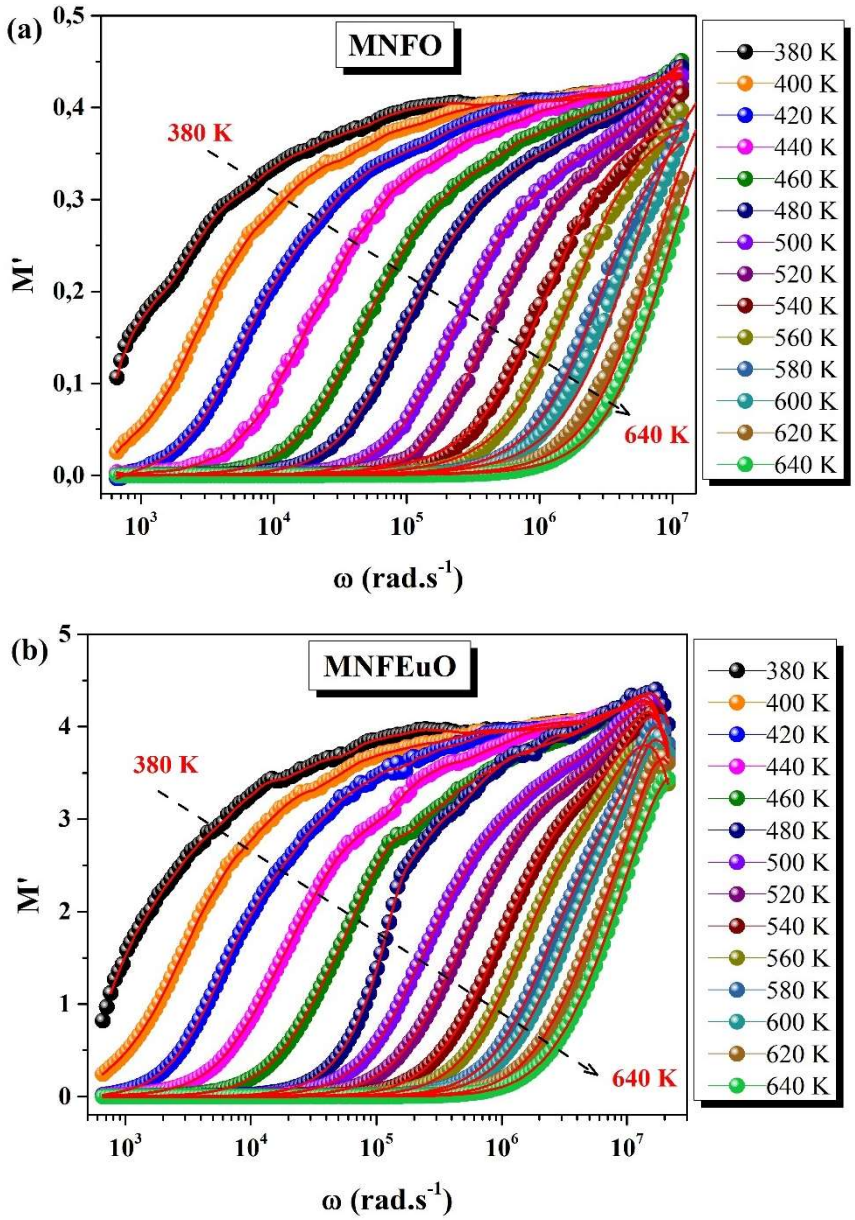
(a)
MNFO
380 K
640 K
M'
ω (rad.s-1)
380 K
400 K
420 K
440 K
460 K
480 K
500 K
520 K
540 K
560 K
580 K
600 K
620 K
640 K
(b)
MNFEuO
380 K
640 K
M'
ω (rad.s-1)
380 K
400 K
420 K
440 K
460 K
480 K
500 K
520 K
540 K
560 K
580 K
600 K
620 K
640 K

Figure 16

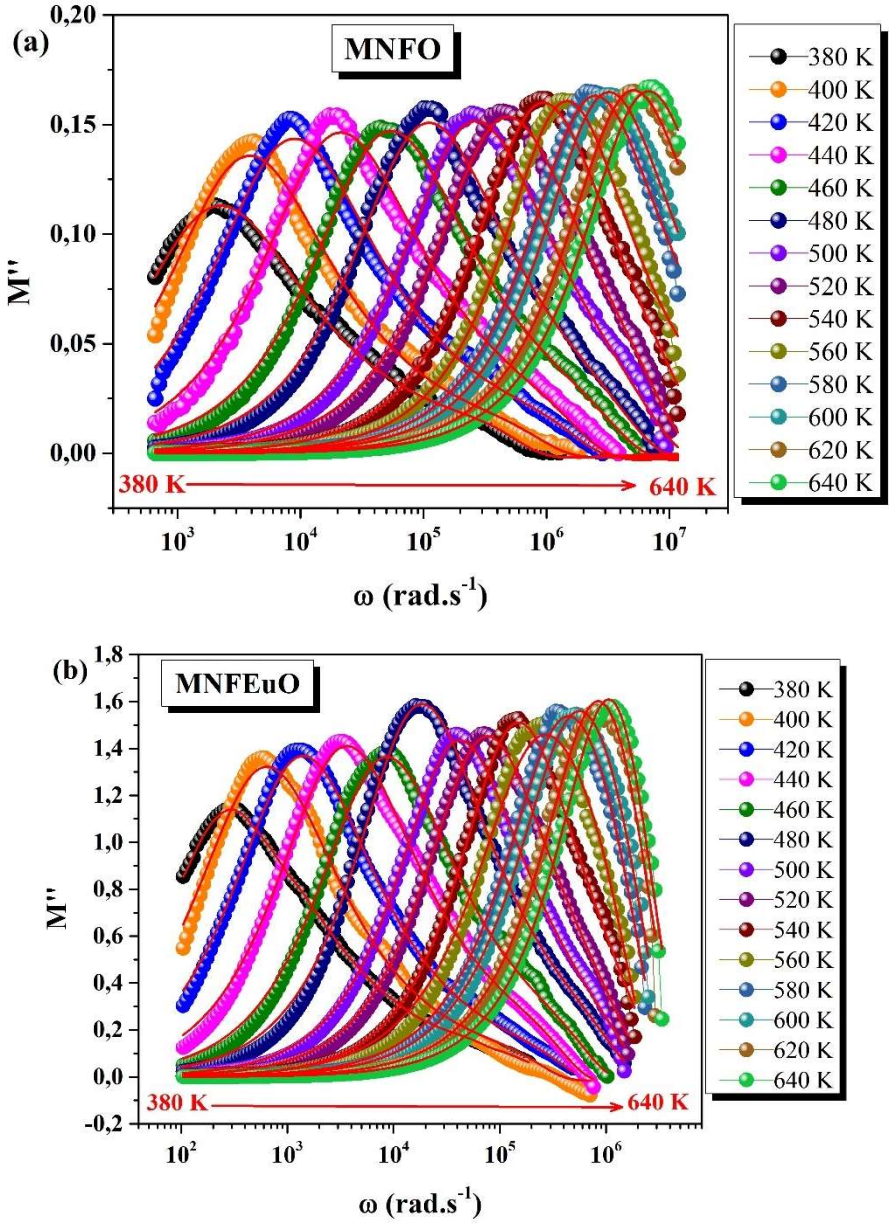
(a)
MNFO
M''
ω (rad.s-1)
380 K
640 K
380 K
400 K
420 K
440 K
460 K
480 K
500 K
520 K
540 K
560 K
580 K
600 K
620 K
640 K
(b)
MNFEuO
M''
ω (rad.s-1)
380 K
640 K

Figure 17

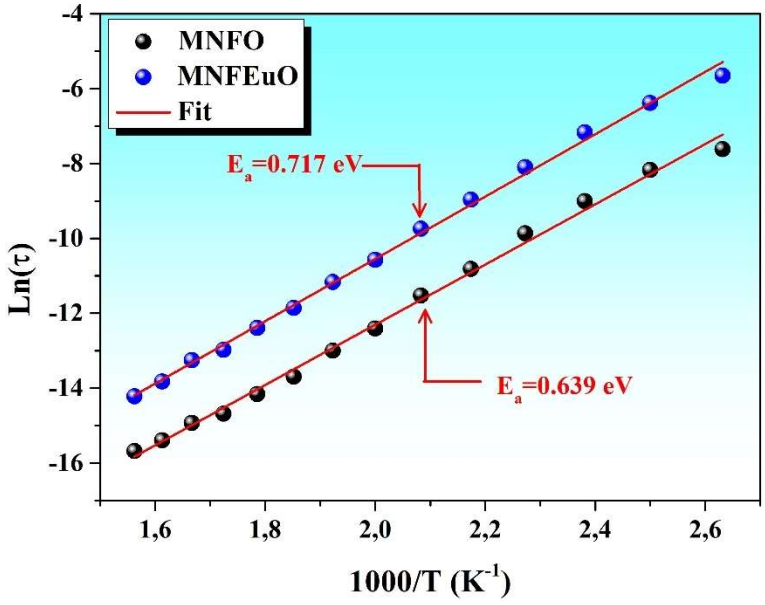

Figure 18

Table 6

T (K)	M_∞	τ (s)	α	γ	β_{KWW}
380	0.2416	4.92×10^{-4}	0.8144	0.8222	0.7218
400	0.2815	2.81×10^{-4}	0.8245	0.8157	0.7243
420	0.2974	1.23×10^{-4}	0.8312	0.8044	0.7209
440	0.2867	5.19×10^{-5}	0.8490	0.7873	0.7207
460	0.2817	2.02×10^{-5}	0.8579	0.7773	0.7193
480	0.2781	9.88×10^{-6}	0.8720	0.7583	0.7144
500	0.2665	4.09×10^{-6}	0.8873	0.7284	0.7013
520	0.2606	2.26×10^{-6}	0.8978	0.6946	0.6812
540	0.2602	1.13×10^{-6}	0.9195	0.6872	0.6885
560	0.2741	7.08×10^{-7}	0.9259	0.7931	0.7780
580	0.2856	4.21×10^{-7}	0.9350	0.7838	0.7767
600	0.2730	3.28×10^{-7}	0.9413	0.7519	0.7550
620	0.2733	2.07×10^{-7}	0.9425	0.7277	0.7360
640	0.2577	1.54×10^{-7}	0.9533	0.6713	0.6957

Table 7

T (K)	M_∞	τ (s)	α	γ	β_{KWW}
380	2.6138	3.50×10^{-3}	0.7790	0.8474	0.7134
400	2.8270	1.69×10^{-3}	0.8253	0.8347	0.7386
420	2.8498	7.70×10^{-4}	0.8361	0.8254	0.7397
440	2.8318	3.03×10^{-4}	0.8379	0.7961	0.7196
460	2.6503	1.28×10^{-4}	0.8510	0.7825	0.7185
480	2.9978	5.90×10^{-5}	0.8696	0.7768	0.7269
500	2.5485	2.57×10^{-5}	0.8927	0.7464	0.7189
520	2.4751	1.42×10^{-5}	0.8983	0.7085	0.6926
540	2.4560	7.09×10^{-6}	0.9237	0.6858	0.6899
560	2.2290	4.14×10^{-6}	0.8424	0.5079	0.5014
580	2.2309	2.31×10^{-6}	0.8686	0.4435	0.4604
600	2.2172	1.75×10^{-6}	0.8721	0.4020	0.4265
620	2.1505	9.90×10^{-7}	0.8871	0.2311	0.2757
640	2.0961	6.68×10^{-7}	0.9144	0.0341	0.0597

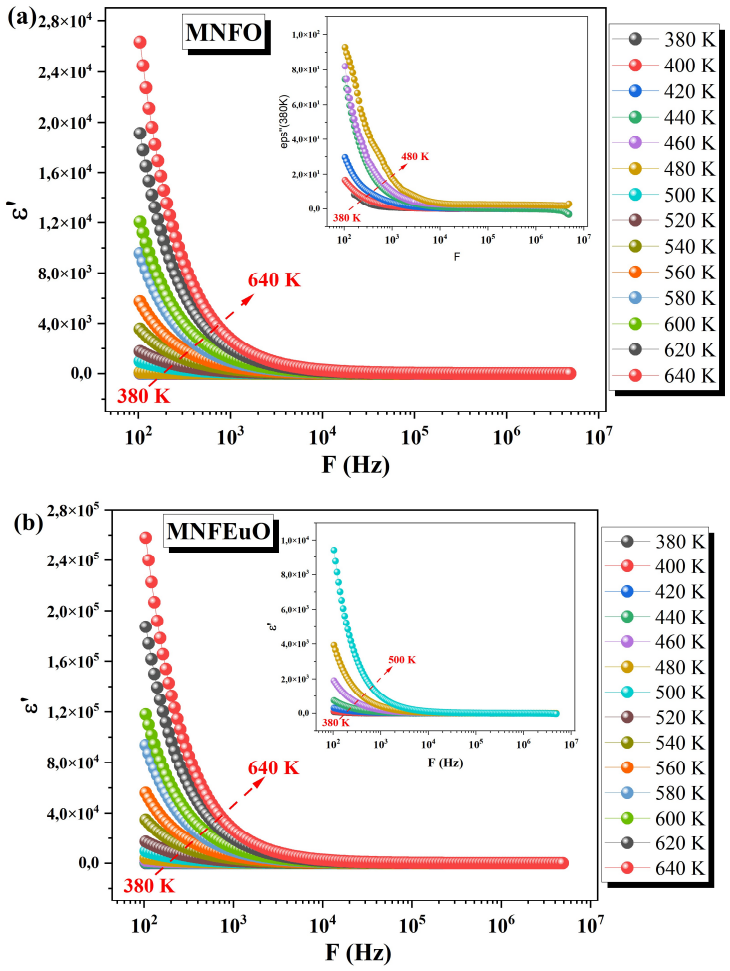
(a)
MNFO
ε'
F (Hz)
640 K
380 K
480 K
eps'(380K)
F
380 K
400 K
420 K
440 K
460 K
480 K
500 K
520 K
540 K
560 K
580 K
600 K
620 K
640 K
(b)
MNFEuO
ε'
F (Hz)
640 K
380 K
500 K
380 K
380 K
400 K
420 K
440 K
460 K
480 K
500 K
520 K
540 K
560 K
580 K
600 K
620 K
640 K

Figure 19

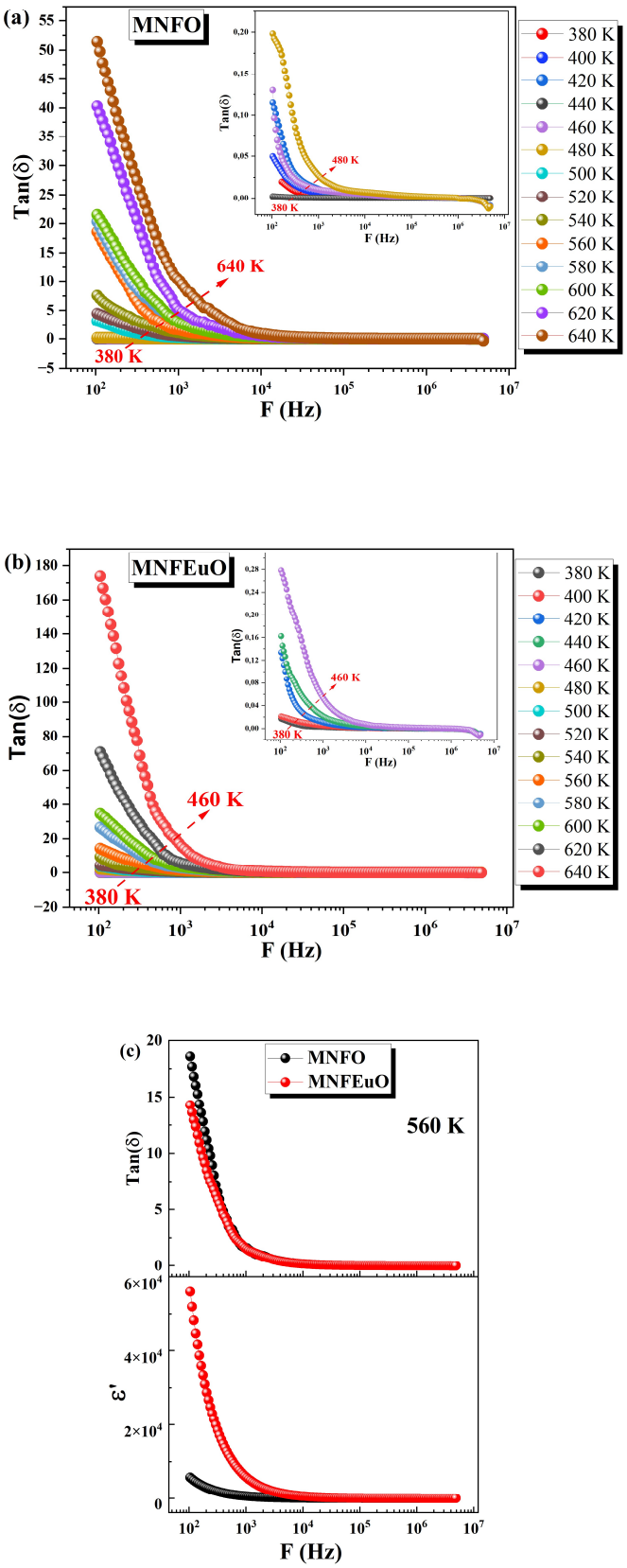
(a)
MNFO
Tan(δ)
F (Hz)
640 K
380 K
480 K
380 K
380 K
400 K
420 K
440 K
460 K
480 K
500 K
520 K
540 K
560 K
580 K
600 K
620 K
640 K
(b)
MNFEuO
Tan(δ)
F (Hz)
460 K
380 K
380 K
400 K
420 K
440 K
460 K
480 K
500 K
520 K
540 K
560 K
580 K
600 K
620 K
640 K
(c)
MNFO
MNFEuO
560 K
Tan(δ)
ε'
F (Hz)

Figure 20